INVESTIGATION OF THERMAL SPREAD DURING ELECTROSURGICAL COAGULATION IN NEUROSURGERY

by

Kuen-Ren Chen

A dissertation submitted in partial fulfillment
of the requirements for the degree of
Doctor of Philosophy
(Mechanical Engineering)
in The University of Michigan
2013

Doctoral Committee:

Professor Albert J. Shih, Chair
Assistant Professor Kira L. Barton
Associate Professor Joseph L. Bull
Professor Katsuo Kurabayashi
Assistant Professor Chia-Ying Lin

ACKNOWLEDGEMENTS

I truly appreciate the countless support and help provided by many people in the way to my degree.

First, I would like to thank my advisor, Professor Albert Shih for giving me this opportunity to come to University of Michigan. He is always there for his students, providing help and guidance for not only research but also career development. His enthusiasm in research and teaching are the key to the finish of my degree. He is very patient with me revising manuscripts and my dissertation. I greatly appreciate his vision that prepares me as a junior researcher in many aspects. Last, I would like thank him for his understanding of my frequent travelling between Ann Arbor and Madison.

I would also like to thank all my committee members, Professors Kira Barton, Joesph Bull, Katsuo Kurabayashi, and Chia-Ying Lin for their guidance and critiquing of my thesis as it progressed. I appreciate their support and advice throughout this entire process. Special thanks to Professor Joesph Bull. Joining his Biotransport lab has inspired me in many ways.

I would like to thank all my fellow lab mates in WuMRC and Biotransport lab. Among them, I must give my deepest thanks to Drs. Robert Dodde and Matthew Chastagner. Without their pioneer work in the field of electrosurgery, I would not have done my study today. In the early years of my Ph.D life, they have been extremely helpful to all my experimental and modeling work. Drs. Bruce Tai and Yancheng Wang are always there when I have all sorts of questions. Dr. Carl McGill, Jorge Sanz-Guerrero, Barry Belmont, and Jeff Plott all provided me numerous supports.

This thesis would also not have been possible without the help of many people from across the University. Drs. Paul Park, Khoi Than, and Anthony Wang of

Neurosurgery Department and Gail Rising from ASOR did a lot of help in all the animal experiments. Many special thanks go to Dr. Roscoe Warner of Pathology Department for the early exploring experiments on mice. Toby Donajkowski has always been a great consultant in terms of machining and mechatronics.

Last but not least, I owe my greatest thank you to my family, especially my lovely wife, Ruby for their support and encouragement. It has not been easy to be apart for Ruby and me throughout these years. We are finally a step forward to be together. Without her patience and understanding, I would not have been able to accomplish this. I love you.

TABLE OF CONTENTS

LIST OF FIGURES

LIST OF TABLES

CHAPTER 1
INTRODUCTION

1.1 Motivation

Electrosurgical coagulation is one of the most important procedures in neurosurgery to control bleeding (Dujovny *et al.*, 1998; Vaellfors and Erlandson, 1980). Bipolar forceps have been developed and applied in neurosurgery clinical practice since 1940s and are the most commonly used device for electrosurgical coagulation (Bulsara *et al.*, 2006). The heat generated in the coagulation process could transfer to the surrounding tissue to cause inadvertent thermal injury, which leads to unfavorable outcomes. As neural tissues are especially vulnerable to heat, having a low threshold temperature of around 43°C and a small amount of required thermal dose for thermal injury (Dewhirst *et al.*, 2003), a better understanding of thermal spread in neurosurgical coagulation procedures is critical and helps to ensure good surgical results. There is a clinical need to understand how to safely use energy-based surgical devices.

Different surgical thermal management techniques, such as control of energy delivery (Sugita and Tsugane, 1974), heat pipe inside the electrode (Arakawa, 2005), and high thermal conductivity coating (Mikami *et al.*, 2007) have been developed to minimize the thermal damage. However, thermal spread of these devices can still exceed 3 mm from the electrode (Sutton *et al.*, 2010; Campbell *et al.*, 2003). The tissue thermal damage can lead to major postoperative issues and is detrimental to a patient's long-term recovery. Such thermal injury to the nerve has been reported clinically (Wallwiener *et al.*, 2010) as well as in animal models (Elliott-Lewis *et al.*, 2010). Given the currently available temperature measurement techniques, tissue temperature during electrosurgery is only available in the surface. The subsurface temperature or thermal injury

information relies on histological analysis. The goal of this study is to gain a better understanding of thermal spread and reduce the thermal injury during the electrosurgical procedure in neurosurgery.

Modeling of the surgical operations is a key to understand the thermal spread. An accurate model not only can provide spatial and temporal temperature distribution but also allows for the calculation of thermal dose to determine the level of thermal injury. Past studies of electrosurgical modeling has focused primarily on tumor ablation within: liver, uterus and heart. In the ablation process, the input voltage is relatively low (<50 V) and the heating times are often on the order of 480 to 720 s (Campbell *et al.*, 2003). The modeling of electrosurgical vessel sealing is much different from the ablation process. It requires more delicate modeling techniques as the vessel sealing process utilizes a high voltage at 100 V in a short time (about 10 s) to occlude the vessel. A model to accurately predict the tissue temperature for bipolar electrosurgery is lacking. The data of tissue thermal and electrical properties, which vary depending on the level of water content, damage, and compression during vessel sealing, is critical for accurate modeling of electrosurgery. The tissue water content is known to be temperature- (Bhattacharya and Mahajan, 2003) and compression-dependent (Dodde *et al.*, 2012). The tissue temperature increases quickly from the resistive heating and the elevated temperature causes irreversible thermal damage. Incorporation of the damage effect into the modeling process has been attempted by altering the specific heat of the tissue (Yang *et al.*, 2007), changing the electrical conductivity of the tissue (Dodde *et al.*, 2008), or by simulating the diffusion of water vapor within the tissue (Abraham and Sparrow, 2007). All these phenomena are important to develop a comprehensive and accurate thermal model.

The knowledge gained from the experiment and model is the foundation to build a clinical simulator for neurosurgeons to practice and understand quantitatively the thermal spread in surgical operations. Most current practices and training programs use supervision of procedures performed on a patient for teaching the neurosurgical procedures. Although there is close supervision of the trainee by a faculty, there is still room for error and it is difficult for a resident or trainee to gain the experience needed. It would be in everyone's best interest if the trainee were able to practice on a clinical simulator to meet an experience threshold before performing procedures on live patients.

One of the barriers for neurosurgical clinical simulator is the phantom with electrical and thermal conductivities of the tissue during electrosurgical coagulation procedures. This will be a key research area in this study.

1.2 Research Objectives and Tasks

The ultimate goal of this study is to achieve effective coagulation with minimal thermal damage. Two objectives are proposed to approach this goal. First is to obtain a comprehensive understanding of thermal spread during coagulation and second is to develop a tissue-mimicking phantom that is able to reproduce temperature response to electrosurgical tools as the biological tissue and can be used to build a clinical simulator.

The specific tasks include:

(1) To investigate the thermal profiles during bipolar coagulation using commercially available bipolar forceps with and without cooling techniques. The heating and cooling effects of each forceps will be compared.

(2) To develop a thermo-electrical model that can accurately predict the temperature distribution during electrosurgery. This model needs to account for evaporation, effects of water loss on tissue properties, and tissue fusion. A fluid phase also needs to be considered as the coagulation is usually performed with the existence of cerebrospinal fluid.

(3) To develop a multi-modality tissue mimicking phantom material for building a clinical simulator for electrosurgery. This phantom material needs to have close mechanical, thermal, and electrical properties as biological tissue.

1.3 Organization of the Dissertation

This dissertation is presented in a multiple manuscript format. Chapters 2, 3, 4, and 5 are written as individual research papers, including the abstract, the main body and the references.

Chapter 2 investigates the thermal profiles of bipolar coagulation on posterior spinal artery in a porcine model with bipolar forceps that incorporate different cooling techniques.

Chapter 3 presents a finite element model (FEM) with the development of thee FEM techniques for modeling of evaporation, water loss, and tissue fusion, to accurately predict tissue temperature during electrosurgical vessel sealing.

Chapter 4 develops a thermo-electrical model, with both solid and liquid phases to calculate tissue temperature during bipolar coagulation of a posterior spinal artery. This model also incorporates the FEM techniques developed in Chapter 3.

Chapter 5 develops a new gellan gum-based multi-modality tissue-mimicking phantom material for electrosurgery. A regression model is developed to allow for the formulation of tissue-mimicking phantom for any targeted soft tissue.

Chapter 6 draws the conclusions and summarizes the original contributions of the dissertation. Several topics and directions are also proposed for future research.

References

Abraham J P and Sparrow E M 2007 A thermal-ablation bioheat model including liquid-to-vapor phase change, pressure-and necrosis-dependent perfusion, and moisture-dependent properties *Int. J. Heat Mass Transfer* **50** 2537-44

Arakawa Y 2005 Application of the bipolar forceps with heat pipe technology (IsoCool) in neurosurgery *Jpn J Neurosurg* **14** 698-705

Bhattacharya A and Mahajan R 2003 Temperature dependence of thermal conductivity of biological tissues *Physiol. Meas.* **24** 769-83

Bulsara K R, Sukhla S and Nimjee S M 2006 History of bipolar coagulation *Neurosurg. Rev.* **29** 93-6

Campbell P A, Cresswell A B, Frank T G and Cuschieri A 2003 Real-time thermography during energized vessel sealing and dissection *Surg. Endosc.* **17** 1640-5

Dewhirst M, Viglianti B, Lora-Michiels M, Hanson M and Hoopes P 2003 Basic principles of thermal dosimetry and thermal thresholds for tissue damage from hyperthermia *Int. J. Hyperthermia* **19** 267-94

Dodde R, Miller S, Geiger J and Shih A 2008 Thermal-electric finite element analysis and experimental validation of bipolar electrosurgical cautery *J. Manuf. Sci. Eng.* **130** 021015-1-8

Dodde R E, Bull J L and Shih A J 2012 Bioimpedance of soft tissue under compression *Physiol. Meas.* **3** 1095-109

Dujovny M, Dujovny N, Gundamraj N R and Misra M 1998 Bipolar coagulation in neurosurgery *Surg. Neurol.* **49** 328-32

Elliott-Lewis E W, Jolette J, Ramos J and Benzel E C 2010 Thermal damage assessment of novel bipolar forceps in a sheep model of spinal surgery *Neurosurgery* **67** 166-72

Mikami T, Minamida Y, Koyanagi I and Houkin K 2007 Novel bipolar forceps with protein repellence using gold-polytetrafluoroethylene composite film *Neurosurgery* **60** 157

Sugita K and Tsugane R 1974 Bipolar coagulator with automatic thermocontrol *J. Neurosurg.* **41** 777-84

Sutton P, Awad S, Perkins A and Lobo D 2010 Comparison of lateral thermal spread using monopolar and bipolar diathermy, the Harmonic Scalpel and the Ligasure *Br. J. Surg.* **97** 428-33

Vaellfors B and Erlandson B E 1980 Damage to nervous tissue from monopolar and bipolar electrocoagulation *J. Surg. Res.* **29** 371-7

Wallwiener C W, Rajab T K, Kramer B, Isaacson K B, Brucker S and Wallwiener M 2010 Quantifying electrosurgery-induced thermal effects and damage to human tissue: An exploratory study with the fallopian tube as a novel in-vivo in-situ model *J Minim Invasive Gynecol* **17** 70-7

Yang D, Converse M C, Mahvi D M and Webster J G 2007 Expanding the bioheat equation to include tissue internal water evaporation during heating *IEEE Trans. Biomed. Eng.* **54** 1382-8

CHAPTER 2
COMPARISON OF THERMAL COAGULATION PROFILES FOR BIPOLAR FORCEPS WITH DIFFERENT COOLING MECHANISMS IN A PORCINE MODEL OF SPINAL SURGERY

ABSTRACT

Objective: Coagulation accomplished using bipolar forceps is common in neurosurgery. Control of thermal spread from the forceps tips into surrounding neural tissues is a persistent concern, as neural tissues are especially vulnerable to heat injury. The purpose of our investigation was to compare the efficacy of cooling mechanisms for four different bipolar forceps and to understand thermal spread when coagulating vessels on the spinal cord.

Methods: Immediately following euthanasia, the dura mater of an ex-vivo porcine model was opened to expose vessels on the spinal cord for coagulation. Temperature profiles were measured at generator power of 25 W and at fixed 5-second activation times. Four bipolar forceps were used in this study, including regular stainless steel, titanium, heat-pipe embedded, and SILVERGlide forceps. The temperature was measured by micro-thermistor at the midpoint between the bipolar tips, and 1 mm and 2 mm away from the midpoint along the center line. Statistical analysis was performed to evaluate the temperature increasing rate.

Results: Temperature profiles indicated that the heat-pipe embedded forceps created the least amount of temperature increase and the highest normalized temperature decreasing slope after activation. The decreasing slope of SILVERGlide forceps is slightly higher than that of regular stainless steel forceps.

Contents of this chapter have been submitted to *Neurosurgery* as Roland K. Chen, Khoi D. Than, Anthony C. Wang, Paul Park, and Albert J. Shih, "Comparison of Thermal Coagulation Profiles for Bipolar Forceps with Different Cooling Mechanisms in a Porcine Model of Spinal Surgery."

Conclusions: Bipolar forceps incorporating either heat-pipe embedded technology or SILVERGlide coating can effectively limit excessive thermal spread, thus decreasing potential injury to adjacent tissues when compared to standard stainless steel and titanium bipolar forceps. Of the two, heat-pipe embedded technology appeared safest as it had better cooling efficiency at higher temperatures.

2.1 Introduction

In neurosurgery, coagulation is an important technique (Vallfors *et al.*, 1980) and is often accomplished using bipolar forceps (Bulsara *et al.*, 2006). However, thermal spread from bipolar tips to adjacent tissue may result in inadvertent thermal injury, leading to unfavorable outcomes in a given operation. As neural tissues are especially vulnerable to heat (Dewhirst *et al.*, 2003), a better understanding of thermal spread in neurosurgical procedures is critical and helps to ensure good surgical results.

The first electrosurgical system developed by Bovie and Cushing in 1926 was monopolar in design. Electrosurgical systems apply high-frequency electrical current to tissues to achieve desired clinical effects, including cutting and coagulating, depending on the applied waveform (Massarweh *et al.*, 2006). A monopolar system requires a returning electrode, which is usually a metal pad placed on the patient's back, to allow for completion of the electrical circuit. The spread of current caused by the returning electrode results in undesired thermal damage to surrounding tissues, which can be especially detrimental in neurosurgery. The concept of bipolar forceps was first presented by Greenwood in 1940 (Greenwood, 1942) and remains the standard configuration to this day. Malis (Malis, 1967) developed the first commercial bipolar coagulation system in the 1960s. This bipolar manner of delivering electrical current to tissue successfully restrains electrical energy and joule heating in a smaller volume of tissue.

This technique is still far from perfect, however, and other existing problems include adherence of tissue to the tips of coagulation forceps, the creation of an electric spark between forceps tips, and the difficulties of removing carbonized clots and tissue from the tips. Most of these complications are due to overheating of the forceps tips (Elliott-Lewis *et al.*, 2009). Numerous attempts have been made to address these

problems. To avoid the adherence of tissue, King and Worpole (King and Worpole, 1972) used continuous saline drip to irrigate the forceps; this irrigation system was later automated by Dujovny et al. (Dujovny *et al.*, 1975). A suction channel added to the irrigation system was modified by Scarff (Scarff, 1974) to moderate bleeding prior to cauterization. Different algorithms to control energy delivery have been developed by different groups (Bergdahl and Vallfors, 1991; Casotto *et al.*, 1988; Sugita and Tsugane, 1974). A variety of coating materials on the tips of bipolar forceps including silver (Jacques *et al.*, 1976), gold (Mikami *et al.*, 2007), nickel (Samii and Dujovny, 1996), and titanium have been tested. Mikami (Mikami *et al.*, 2004) compared forceps made of three different materials (gold, stainless steel, and titanium) and concluded that gold-plated forceps have the least amount of adhered coagulum. Another technique, active heat transfer (AHT), uses fluid-filled heat pipes to continuously transfer heat away from the bipolar tips and has been shown to reduce excessive heat buildup and minimize thermal spread (Arakawa, 2005).

While overheating is an important issue that leads to other problems such as adherence and thermal damage, there has been a paucity of research examining thermal spread. Elliot-Lewis et al. (Elliott-Lewis and Benzel, 2010; Elliott-Lewis *et al.*, 2009) compared resultant temperatures for IsoCool bipolar forceps that incorporate AHT (by Codman & Shurtleff, Warsaw, IN) and conventional anti-stick bipolar forceps. Temperature was measured by thermocouple with a 1 Hz sampling rate and estimated by infrared thermal imaging. The experiment was performed in ex-vivo bovine liver and in-vivo rat brain. Another study compared thermal damage between devices in sheep spines and showed that AHT forceps caused significantly less thermal-damaged area; however, the temperature was not measured (Elliott-Lewis *et al.*, 2010).

Thermal profiling on a spinal model with higher temporal resolution is still needed to assess thermal spread more accurately. Our study was designed to compare thermal profiling using bipolar forceps with different cooling mechanisms, including AHT, SILVERGlide coating, as well as traditional stainless steel and titanium forceps.

2.2 Materials and Methods

The experiment was conducted in an animal surgery operating room at the University of Michigan Medical School. The procedure was compliant with the protocol approved by the University Committee on Use and Care of Animals (UCUCA). Two euthanized pigs (50% Duroc, 25% Yorkshire, and 25% Landrace) weighing 50 kg were used in this study.

Four different bipolar forceps were compared: (1) regular stainless steel bipolar forceps (DePuy Codman & Shurtleff, Warsaw, IN); (2) titanium bipolar forceps (Covidien, Boulder, CO), (3) AHT: IsoCool bipolar forceps (DePuy Codman & Shurtleff); and (4) SILVERGlide bipolar forceps (Stryker, Kalamazoo, MI). The tips of these four forceps are shown in Figure 2.1.

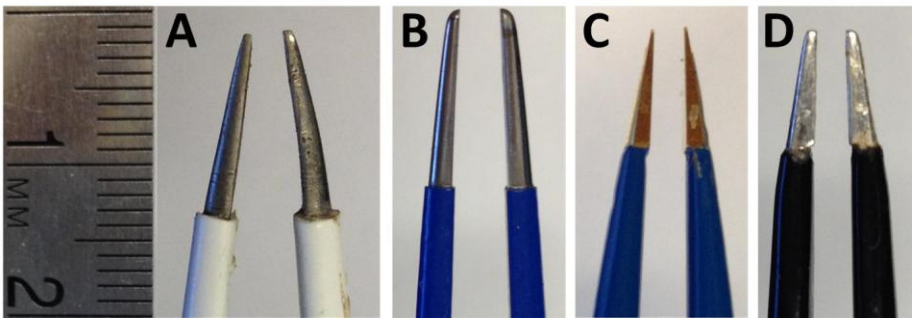

Figure 2.1 Tips of forceps used in this study. A: regular stainless steel, B: titanium, C: AHT, D: SILVERGlide

The titanium bipolar forceps are lighter in weight so that it is more comfortable for neurosurgeons to operate and also allows for a better control of motion. However, titanium has a lower thermal conductivity than stainless steel and thus cannot conduct the heat away as efficiently. The IsoCool bipolar forceps have embedded heat pipes within the shafts of the bipolar forceps to actively transfer heat away from its tips. The heat pipes contain a two-phase working fluid. The fluid is evaporated in the distal end and diffuses to the proximal end with cooler temperatures. The vapor then condenses to liquid and flows back to the distal end. This phase-exchanging cycle is effective for heat transfer. The SILVERGlide bipolar forceps are made of stainless steel with tips coated in a silver alloy. The high thermal conductivity of the silver alloy conducts heat away faster than regular uncoated stainless steel forceps. The chemical inertia of the silver alloy also prevents tissue adherence or charring; thus, the SILVERGlide forceps are also known as

anti-stick forceps. All four forceps were powered by the same electrosurgical generator, Valleylab Force FX (Covidien). The power was set to 25 W for all trials.

A real-time subsurface temperature measurement technique developed by Dodde et al. (Dodde *et al.*, 2009) was used in our study. We used micro-thermistors (Model #56A1002-C8; Alpha Technics, Irvine, CA) that have an outside diameter of 0.46 mm. The measurement tolerance is ± 0.1°C at 25°C with a time constant of 250 ms. Voltage differences across thermistors were recorded using a Wheatstone bridge circuit, and the signals were transmitted and converted to temperatures using LabVIEW System Design Software (National Instruments, Austin, TX) via a data acquisition system (PXI-1033; National Instruments). The sampling rate was 100 Hz. A low-pass resistance-capacitance (RC) filter with cutoff frequency of 3.38 Hz at 25°C (R: 10 kΩ and C: 4.7 μF) was connected to each Wheatstone bridge to eliminate high-frequency noise induced by the electrosurgical generator and the 60 Hz alternating current noise. Polycarbonate fixtures were created for each of the forceps tested to ensure temperature measurements were recorded at precise locations (Figure 2.2, A). As illustrated in Figure 2.3, all three measuring positions were along the center line between the tips of the forceps and were either midpoint (thermistor #1), 1 mm (thermistor #2), or 2 mm (thermistor #3) away from the midpoint along the center line of the forceps tips. The forceps tips were fixed with 2 mm spacing by use of another fixture, as shown in Figure 2.2, B.

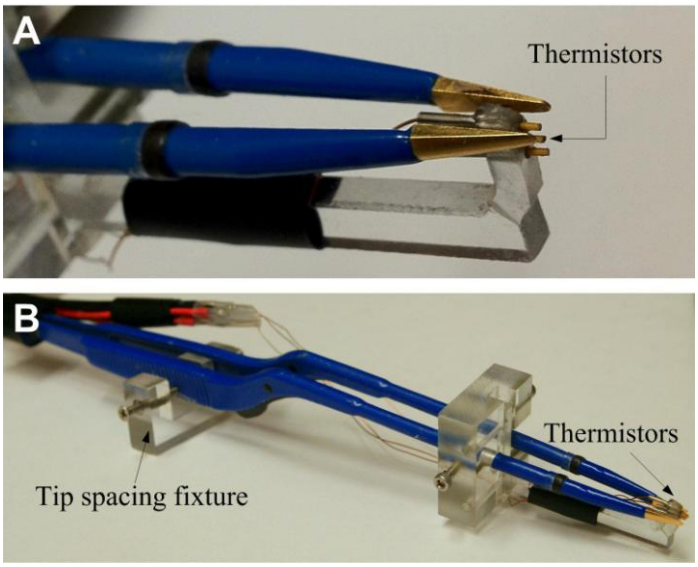

Figure 2.2 Photographs of bipolar forceps showing fixture for thermistors (A) and tip spacing fixture (B).

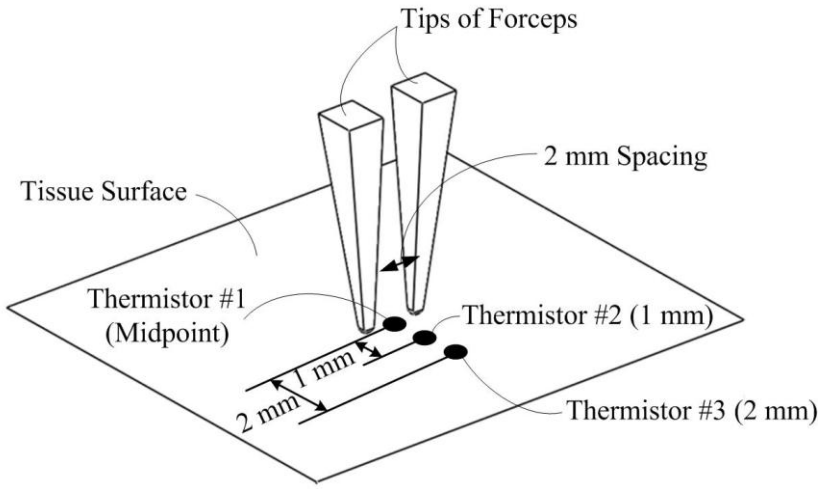

Figure 2.3 Schematic illustration of temperature measurement points

The experiment was carried out immediately after euthanizing the pig. This ex-vivo experimental setup for biopolar coagulation was consistent for all tests. The goal was to compare the thermal profiles of four forceps under the same condition. In this regard, the ex-vivo porcine spinal cord configuration was adequate to achieve this goal. A neurosurgeon opened the dura mater to expose vessels on the spinal cord, as shown in Figure 2.4. Vessels with a diameter between 0.3 to 0.5 mm were chosen to be coagulated. Prior to each bipolar coagulation, the spinal cord was irrigated with water to maintain proper moisture on the spinal cord surface. The power of the generator was set at 25 Malis™ units (which corresponds to a root mean square of 61 V). Activation time of the generator was fixed at 5 seconds to simulate a moderate coagulating situation (Arakawa, 2005). The order of coagulation was randomized to neutralize any experimental uncertainty.

The number of coagulation attempts was determined based on a preliminary study; a total sample size of n = 24 (six trials per forceps) was required to achieve statistical power 95% (Faul et al., 2009). In this study, 36 trials were conducted (9 per forceps). Three one-way ANOVA analyses were carried out to examine whether the temperature at 5 seconds among the four forceps varied, for three measurement points each. Differences indicated by the ANOVA analyses were tested using the Tukey-HSD test for post hoc multiple comparisons. Statistical significance was set at $p < 0.05$. All analyses were performed with SPSS for Windows, version 20 (IBM Corp, 2011).

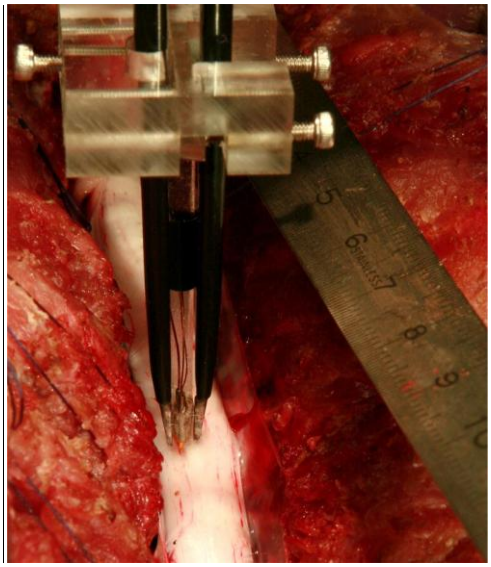

Figure 2.4 Photograph showing process of coagulating a vessel on the spinal cord of a porcine model

2.3 Results

Figure 2.5 shows temporal temperature at the three thermistor locations using the four bipolar forceps during coagulation of vessels on the spinal cord. Each temperature curve is the average result of the two coagulations. The starting internal temperature of the porcine spinal vessel was 25°C. For thermistor #1, the temperature increased about 34°C, 30°C, 15°C, and 8°C for the regular, titanium, AHT, and SILVERGlide forceps, respectively, at the end of each 5-second activation cycle. The temperature then dropped after activation. Temperature of the regular forceps decreased most rapidly, as it had the greatest temperature gradient to the ambient environment. For thermistor #2, the temperature increased by about 24°C, 21°C, 10°C, and 6°C for regular, titanium, AHT, and SILVERGlide forceps, respectively, at the end of the activation. Temperature of all these four devices then kept increasing slowly for about another 1 second demonstrating that heat was still being conducted from the midpoint. For thermistor #3, temperature of the regular and SILVERGlide devices increased over the whole 10-second recording period, while temperature of the AHT device remained at roughly the same level after activation.

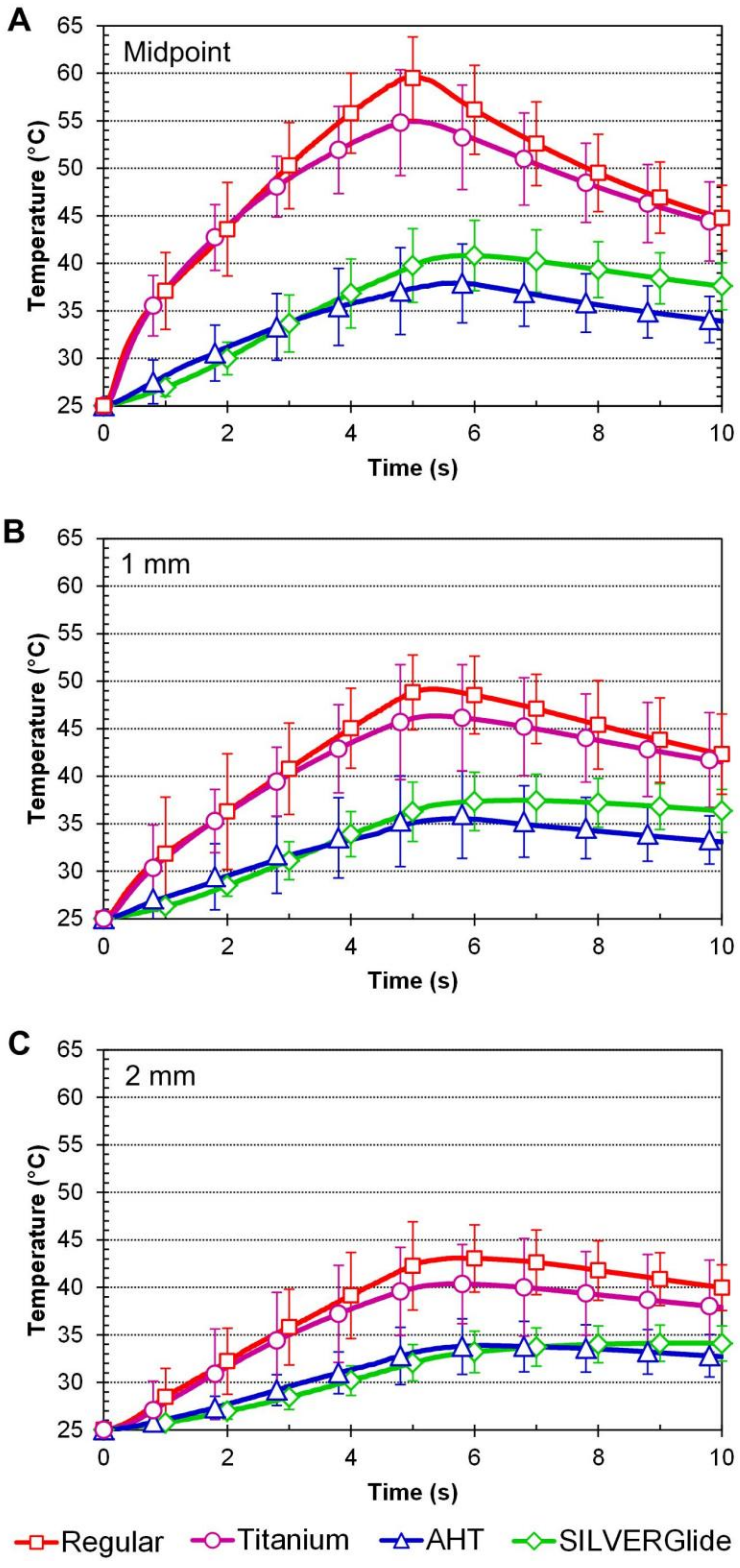

Figure 2.5 Line graphs illustrating temporal temperature profiles at the three measuring positions: A, midpoint; B, 1 mm; and C, 2 mm away from midpoint along the center line

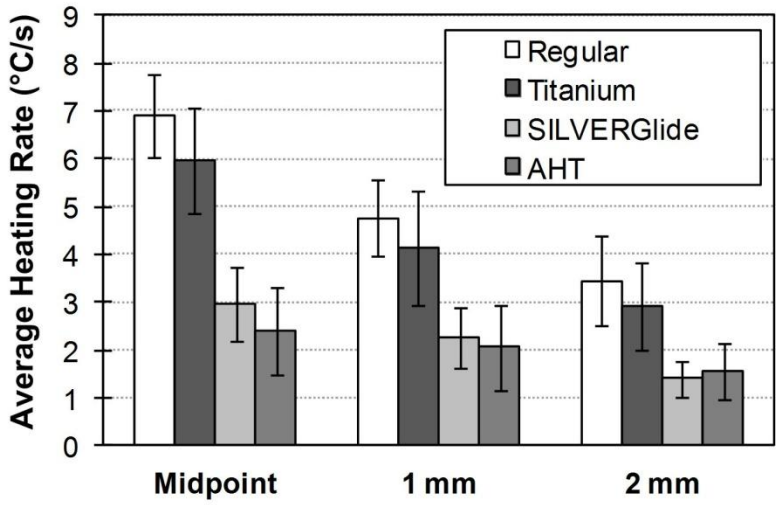

Figure 2.6 Temperature increase at the 5th second for the three measurement positions

Figure 2.6 compares the averaged heating rate (°C/s) for all three measurement points among the four forceps. The three one-way ANOVA analyses showed that the temperature increasing rate significantly varied among forceps for all three measurement points (midpoint: $F_{(3, 32)} = 37.1$, $p < 0.001$, 1 mm: $F_{(3, 32)} = 14.7$, $p < 0.001$, and 2 mm: $F_{(3, 32)} = 10.7$, $p < 0.001$). Post hoc multiple comparison tests were then carried out to compare the difference of temperature-increasing rate between any pair of forceps. The regular stainless steel forceps had significantly higher temperature-increasing rate than both AHT forceps and SILVERGlide forceps for all three measurement points (Tukey's HSD, midpoint: $p < 0.001$ and $p < 0.001$, 1 mm: $p < 0.001$ and $p < 0.001$, 2 mm: $p < 0.001$ and $p = 0.001$, respectively). The titanium forceps also had significantly higher temperature-increasing rate than AHT forceps and SILVERGlide forceps for all three measurement points (Tukey's HSD, midpoint: $p < 0.001$ and $p < 0.001$, 1 mm: $p = 0.003$ and $p = 0.001$, 2 mm: $p = 0.007$ and $p = 0.024$, respectively). There was no difference between the regular stainless steel forceps and the titanium forceps for all three measurement points. There was also no difference between the AHT forceps and the SILVERGlide forceps for all three measurement points.

2.4 Discussion

In this study, we compared temperature profiles when coagulating vessels on porcine spinal cord using bipolar forceps with different cooling mechanisms. The results provide a clear comparison among the four devices studied. The regular stainless steel forceps produced the highest temperatures at all three thermistor locations. The AHT forceps had the least temperature increases at all three locations. The temperature resulting from titanium forceps is slightly lower than the regular stainless steel forceps. The SILVERGlide forceps showed slightly higher temperature increases than the AHT forceps. The AHT forceps, which uses heat pipes, effectively conduct heat away from the tips.

As indicated by the ANOVA analyses, the AHT and SILVERGlide forceps have significantly slower temperature increasing rate compared to the regular stainless steel and titanium forceps. This slow temperature increase may be contributed to two factors, the efficiency of the forceps to convert electrical energy to thermal energy and the effect of cooling mechanisms. These two factors will be discussed in the following paragraphs. The slow temperature-increasing rate means a better control of coagulation and less tendency of overheating tissue.

Electrical energy converts into thermal energy following Joule's First Law. In the case of bipolar forceps, Joule heating occurs mostly in the region between the bipolar tips. Although the power setting for each forceps was the same, the resulting temperatures had large differences. The major difference may be contributed to the efficacy of Joule heating for each forceps but not the efficiency of cooling. According to Joule's first law and Ohm's law, $P=V^2/R$, where P is the energy converted from electrical energy to thermal energy, V is the supplied voltage, and R is the electrical resistance between the bipolar forceps. Given the same voltage supply V (power setting), the larger the R is, the less electrical energy is converted to thermal energy. As R is related to the contact area between the forceps tips and the tissue being coagulated, a larger contact area leads to smaller R and is more capable to generate heat. While the AHT forceps have the smallest tips (as shown in Figure 2.1), it can be expected that the least amount of heat and lowest temperature will be generated by the AHT forceps.

After the activation stops, the generated heat then transfers away from the coagulation region via three pathways. First, heat can be conducted into adjacent tissue. Second, it can be absorbed by the forceps itself. Third, the heat can be diffused into the ambient surroundings. Figure 2.7 shows the temperature changes after the 5 seconds activation. The slope of each curve is the temperature-descending rate via these three pathways. The slopes of regular stainless steel and titanium forceps are steeper because these two forceps have higher temperature gradients (i.e. the temperature difference between the midpoint and 1 mm). It is known that the rate of heat conduction is proportional to the temperature gradient (Incropera and DeWitt, 2002). The slope of regular stainless steel forceps is slightly higher than that of titanium forceps because stainless steel has higher thermal conductivity than titanium and can conduct heat more efficiently. The AHT and SILVERGlide forceps have lower slope due to the smaller temperature gradient. On the other hand, the temperature of AHT and SILVERGlide forceps continued increasing for about 0.5 second after the activation stopped. This is because the heat transferring from the tissue around the tips to the midpoint between the tips is larger than that of the heat conducting to the tissue that is far from the tips.

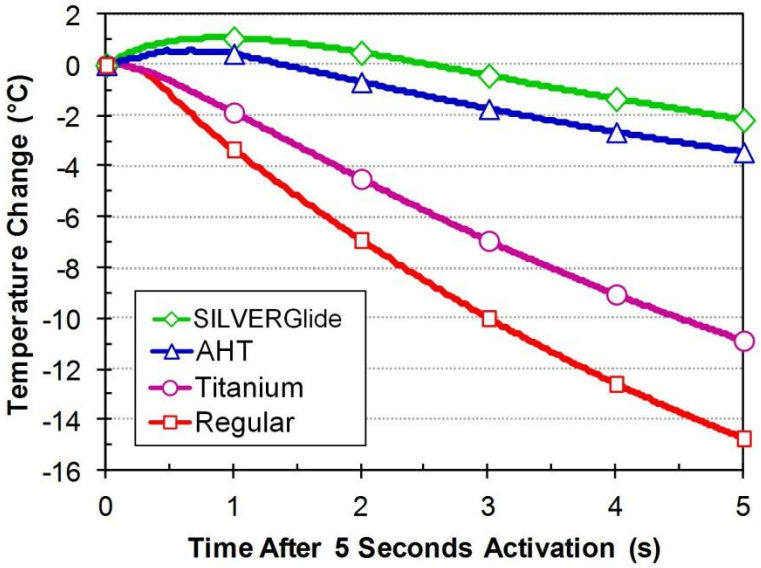

Figure 2.7 Temperature changes after 5 seconds activation

The AHT forceps work by the two-phase working fluid vacuum-sealed in the heat pipes that are embedded in the forceps shafts (Elliott-Lewis and Benzel, 2010; Elliott-

Lewis *et al.*, 2009). The fluid has a working temperature range which varies by the type of fluid and the level of vacuum (Zohuri, 2011). The working fluid also needs time to accumulate enough energy to overcome the latent heat to evaporate the working fluid. Before the temperature reaches the working range, the fluid inside the heat pipe cannot be evaporated and thus the AHT forceps do not show a superior performance below this working temperature range. As shown in Figure 2.5A, for the first three seconds, the temperature of AHT forceps was higher than that of SILVERGlide forceps. This is because the silver coating on the surface of SILVERGlide forceps has a higher thermal conductivity than that of the AHT forceps. Before the heat pipe of the AHT forceps reaches the working temperature, the SILVERGlide forceps have a better performance to conduct the heat away. Once the temperature reaches the working range, the AHT forceps can then conduct heat more efficiently.

Results of our study performed on porcine spinal cord are consistent with the results obtained in a previous study on coagulation in ex vivo calf liver (Elliott-Lewis *et al.*, 2009). In spinal surgery, neurosurgeons tend to use a lower power setting to prevent thermal damage. We used 25 Malis units for our study, while previous studies (Elliott-Lewis and Benzel, 2010; Elliott-Lewis *et al.*, 2009) used much higher power at 35 and 50 Malis units. It can be expected that with a higher power, a larger temperature difference among devices can be seen. However, using a low power setting, we still found noticeable differences.

The major limitation of this study is that the experiment was not conducted with live animals. Thus, the efficacy of coagulation could not be studied. However, the main purpose of this study was to compare the temperature profiles and the effect of cooling mechanisms. For the AHT device, the low temperatures generated may not coagulate the vessel effectively, thereby requiring a longer activation time. This may be a concern for neurosurgeons and requires further study.

2.5 Conclusions

Based on this porcine spinal cord study, the AHT and SILVERGlide forceps produced a less amount of thermal spread compared to regular stainless steel and titanium forceps. The AHT and SILVERGlide forceps also show a slower temperature-increasing rate which allows a better control of temperature increase, but may require longer

coagulation time. The stainless steel and titanium forceps have a higher temperature-increasing rate and are better in the case of heavy bleeding. The AHT forceps have best cooling efficiency among the four compared forceps at higher temperature. Therefore, it would appear to be safer to use AHT forceps when hemostasis needs to be performed adjacent to vital neural tissues. Future study may incorporate external cooling device to stainless steel or titanium forceps to maintain the ability to coagulate vessel quickly and minimize thermal damage to the adjacent tissue.

References

Arakawa Y 2005 Application of the bipolar forceps with heat pipe technology (IsoCool) in neurosurgery *Jpn J Neurosurg* **14** 698-705

Bergdahl B and Vallfors B 1991 Studies on coagulation and the development of an automatic computerized bipolar coagulator. Technical note *J Neurosurg* **75** 148-51

Bulsara K R, Sukhla S and Nimjee S M 2006 History of bipolar coagulation *Neurosurg Rev* **29** 93-6

Casotto A, Castrioto C and Orvieto P 1988 An advanced system for electrocoagulation in neurosurgery *J Neurosurg Sci* **32** 61-3

Dewhirst M W, Viglianti B L, Lora-Michiels M, Hanson M and Hoopes P J 2003 Basic principles of thermal dosimetry and thermal thresholds for tissue damage from hyperthermia *Int J Hyperthermia* **19** 267-94

Dodde R, Shih A and Advincula A P 2009 A novel technique for demonstrating the real-time subsurface tissue thermal profile of two energized surgical instruments *J Minim Invasive Gynecol* **16** 599-603

Dujovny M, Vas R, Osgood C P, Maroon J C and Janetta P J 1975 Automatically irrigated bipolar forceps. Technical note *J Neurosurg* **43** 502-3

Elliott-Lewis E W and Benzel E C 2010 Thermal comparison of novel bipolar forceps in bovine liver *Neurosurgery* **67** 160-5

Elliott-Lewis E W, Jolette J, Ramos J and Benzel E C 2010 Thermal damage assessment of novel bipolar forceps in a sheep model of spinal surgery *Neurosurgery* **67** 166-72

Elliott-Lewis E W, Mason A M and Barrow D L 2009 Evaluation of a new bipolar coagulation forceps in a thermal damage assessment *Neurosurgery* **65** 1182-7

Faul F, Erdfelder E, Buchner A, and Lang A G 2009 Statistical power analyses using G*Power 3.1: Tests for correlation and regression analyses. *Behav Res. Methods*, **41**, 1149-1160.

Greenwood J, Jr. 1942 Two point coagulation: a follow-up report of a new technic and instrument for electrocoagulation in neurosurgery *Arch Phys Ther* **23** 552-4

IBM Corp. Released 2011. IBM SPSS Statistics for Windows, Version 20.0. Armonk, NY: IBM Corp

Incropera F P and DeWitt D P 2002 *Fundamentals of Heat and Mass Transfer*, (New York: Wiley)

Jacques S, Bullara L A and Pudenz R H 1976 Microvascular bipolar coagulator. Technical note *J Neurosurg* **44** 523-4

King T T and Worpole R 1972 Self-irrigating bipolar diathermy forceps. Technical note *J Neurosurg* **37** 246-7

Malis L I 1967 *Micro-Vascular Surgery: Report of First Conference, October 6-7, 1966, Mary Fletcher Hospital, Burlington, Vermont,* ed R M Donaghy Peardon and M G Yasargil (St. Louis: C. V. Mosby Co.) pp 126-30

Massarweh N N, Cosgriff N and Slakey D P 2006 Electrosurgery: history, principles, and current and future uses *J Am Coll Surg* **202** 520-30

Mikami T, Minamida Y, Koyanagi I and Houkin K 2007 Novel bipolar forceps with protein repellence using gold-polytetrafluoroethylene composite film *Neurosurgery* **60** ONS157-61

Mikami T, Takahashi A, Hashi K, Gasa S and Houkin K 2004 Performance of bipolar forceps during coagulation and its dependence on the tip material: a quantitative experimental assay. Technical note *J Neurosurg* **100** 133-8

Samii A and Dujovny M 1996 Kirwan "non-stick" bipolar forceps *Surg Neurol* **45** 297-8

Scarff T B 1974 A new bipolar suction-cautery forceps for micro-neurosurgical use *Surg Neurol* **2** 213

Sugita K and Tsugane R 1974 Bipolar coagulator with automatic thermocontrol. Technical note *J Neurosurg* **41** 777-9

Vallfors B, Erlandson B E, Wieck B O, Hansson H A and Svensson J 1980 Coagulation in neurosurgery *Acta Neurochir (Wien)* **55** 29-34

Zohuri B 2011 Heat Pipe Design and Technology: a Practical Approach (Boca Raton: CRC Press)

CHAPTER 3

ELECTROSURGICAL VESSEL SEALING TISSUE TEMPERATURE: EXPERIMENTAL MEASUREMENT AND FINITE ELEMENT MODELING

ABSTRACT

The temporal and spatial tissue temperature profile in electrosurgical vessel sealing was experimentally measured and modeled using finite element modeling (FEM). Vessel sealing procedures are often performed near the neurovascular bundle and may cause collateral neural thermal damage. Therefore, the heat generated during electrosurgical vessel sealing is of concern among surgeons. Tissue temperature in an in-vivo porcine femoral artery sealed using a bipolar electrosurgical device was studied. Three FEM techniques were incorporated to model the tissue evaporation, water loss, and fusion by manipulating the specific heat, electrical conductivity, and electrical contact resistance, respectively. These three techniques enable the FEM to accurately predict the vessel sealing tissue temperature profile. The averaged discrepancy between the experimentally measured temperature and the FEM predicted temperature at three thermistor locations is less than 7%. The maximum error is 23.9%. Effects of the three FEM techniques are also quantified.

Contents of this chapter have been accepted by *IEEE Transaction on Biomedical Engineering* as Roland K. Chen, Matthew W. Chastagner, Robert E. Dodde, and Albert J. Shih, "Electrosurgical Vessel Sealing Tissue Temperature: Experimental Measurement and Finite Element Modeling."

3.1 Introduction

Electrosurgery was developed to ablate tumors (Goldberg, 2001), cauterize tissue (Pearce and Thomsen, 1992), and to seal vessels (Newcomb *et al.*, 2009) by delivering electrical current (frequency ranges from 300 to 550 kHz) to tissue. The electrosurgical devices used for vessel sealing work by clamping down on the vessel while applying an electrical current through the tissue. The resistive heating generated by the applied current increases the tissue temperature. This elevated temperature causes the proteins within the tissue to denature and hence form a seal (Wright and Humphrey, 2002). Electrosurgical devices have been proven to safely and effectively seal vessels (Campagnacci *et al.*, 2007; Ponsky *et al.*, 2009). The advantages of using electrosurgical devices over conventional vessel ligation include less operative time (Heniford *et al.*, 2001; Shen *et al.*, 2005) and shorter postoperative hospital stay (Campagnacci *et al.*, 2007).

Despite these advantages, potential thermal damage to adjacent nerves surrounding the sealing site is of concern for surgeons, particularly in procedures such as prostatectomy, spinal surgery, and brain surgery. In prostatectomy, bipolar forceps are usually only used to control heavy bleeding due to the potential of thermal damages to the neurovascular bundle. In neurosurgery, bipolar forceps are used to coagulate vessels right on the spinal cord or cerebral cortex, which have a low temperature threshold before thermal damage occurs, around 43°C (Dewhirst *et al.*, 2003). Since the tissue must be heated to seal the vessel, the adjacent tissue is at risk of thermal damage because of the thermal spread from the sealing site.

Most of the current electrosurgical devices attempt to reduce thermal spread through the use of generators that implement control algorithms for the energy output (Kennedy *et al.*, 1998). In addition, other techniques used to minimize thermal spread include "smart electrodes" that turn on and off depending on the local tissue temperature (Smaldone et al., 2008) and a heat pipe embedded within the electrode for cooling (Vellimana et al., 2009). However, even with these advanced techniques, the thermal damage from these devices often exceeds 3 mm from the edge of electrode (Campbell et al., 2003). The thermal damage to the neural tissue can lead to major postoperative issues and can be detrimental to a patient's long-term recovery.

To prevent thermal damage and improve patient safety, a better understanding of the thermal spread in electrosurgical vessel sealing is needed. Modeling the sealing process is key to this because it provides more insight into the thermal spread. Previous studies on electrosurgical modeling focused primarily on tumor ablation within the liver (Haemmerich et al., 2003), uterus (Martin and Angelone, 2009), and heart (Tungjitkusolmun et al., 2000). However, modeling electrosurgical vessel sealing is different from modeling the ablation process. In the ablation process, the energy power level being delivered is relatively low (<50 V) and the heating times are often on the order of 480 to 720 s. In contrast, the vessel sealing process utilizes a relatively high voltage (about 100 V) in a shorter time (about 10 s) to occlude the vessel. Dodde et al. (Dodde et al., 2008) has developed a model to predict the thermal spread in cauterizing spleen tissue from a bipolar electrosurgical device that uses similar voltage and activation time in the vessel sealing process. This model needs to be further modified to predict the thermal spread in the vessel sealing process because of three major challenges: 1) the phase change via evaporation and the associated energy of latent heat, 2) the change of tissue electrical conductivity due to water loss, and 3) the contact resistance (CR) in the interfacial surface of the vessel. These challenges can be overcome by manipulating the material properties used in the finite element modeling (FEM) to account for those phenomena of evaporation, water loss, and tissue fusion.

Accurate thermal and electrical properties are critical for modeling electrosurgical vessel sealing. The tissue's thermal and electrical properties vary with factors including temperature (Golombeck et al., 1999; Berjano, 2006), water content (Yang et al., 2007a), thermal damage (Haemmerich et al., 2003), phase change, and compression (Dodde et al., 2012). To our knowledge, such a comprehensive model which incorporates temperature, water content, thermal damage, phase change, and compression is yet to be developed.

The present study, therefore, aims to develop an experimentally validated model to predict the spatial and temporal distributions of tissue temperature during the electrosurgical vessel sealing process. A bipolar electrosurgical device is used to perform the vessel sealing while thermistors are used to measure the tissue temperature during the process. A FEM incorporating the changes in material properties in a vessel during

electrosurgical sealing is developed. The model is then validated by the experimental results and the effects of the manipulated material properties are investigated.

3.2 Experimental Setup

An *in-vivo* porcine model (Figure 3.1(a)) was used for measuring the temperature profile during a vessel sealing process. In this experiment, a 3 mm diameter femoral artery was sealed by a 5 mm bipolar electrosurgical device, as shown in Figure 3.1(b). The temperature profile was measured by micro thermistors. The electrical input from the electrosurgical device to the sealing site was also measured.

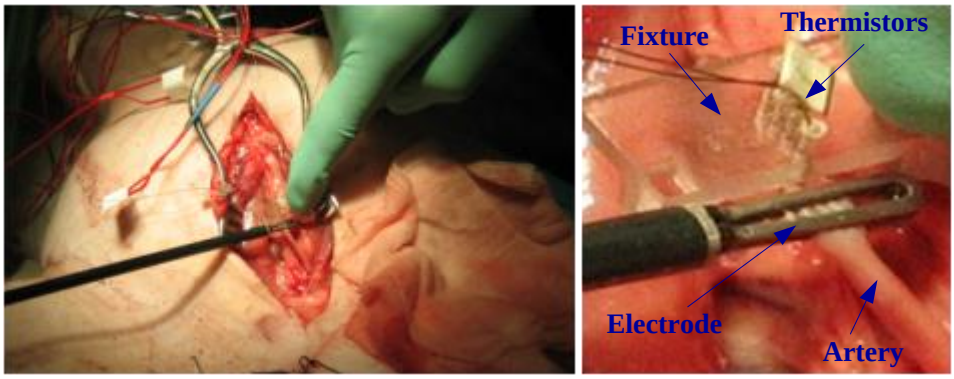

(a) (b)

Figure 3.1 The bipolar electrosurgical device used in this study and (b) a close-up view of electrode tip and temperature measurement setup

A porcine (50% Duroc, 25% Yorkshire, and 25% Landrace) model weighing 45 kg was used in this experiment. The experiment was conducted at the University of Michigan Medical School under an approved animal protocol. Anesthesia was induced in the animal with an intramuscular injection of Telazol® (6 mg/kg) mixed with Xylazine (2.2 mg/kg). The animal was intubated and placed under general anesthesia using Isoflurane (2 to 2.5%). The animal was then placed on a ventilator (10 ml/kg) at 12 bpm. Oxygen saturation, pulse rate, and respiratory rate were monitored with pulse oximetry at regular intervals.

A 5 mm bipolar cutting forceps (Gyrus ACMI, Olympus #3005PK) was used to seal the vessel. The device was powered by a generator (Gyrus ACMI, Olympus, SuperPulse Generator #744000), which was set to the VP1 setting with a power level of 30 W. Generator activation was stopped once the audible tone from the generator was

heard. The leads of the device were attached to a digital oscilloscope (Agilent #54833A) in peak detect mode with a 100:1 high voltage probe (Agilent 10076A) and a current probe (Agilent 1147A). The voltage data was collected at 10 kHz.

Tissue temperature was measured using a series of micro thermistors (Alpha Technics Model #56A1002-C8) set into a polycarbonate fixture, as shown in Figure 3.1(b). The polycarbonate fixture, epoxied to the top of the electrodes, held the thermistors in positions relative to the edge of the electrode. Three thermistors were epoxied into the fixture with the tip exposed to a depth of 0.75 mm. In the fixture, the distances between the edge of the electrode and the thermistors were 1.0, 2.0, and 3.0 mm. The thermistors used in this study have an outside diameter of 0.46 mm, a time constant of 250 ms, and an accuracy of ±0.1°C at 25°C. It is assumed that the thermistors would not interfere the electrical current as its size is small. A data acquisition system sampling at 40 Hz was utilized to record temperature data. A 3 Hz low pass filter and a moving average with a 15 data point window size were applied to the experimental data to remove the electrical noise.

3.3 Finite Element Modeling

A FEM for bipolar electrosurgical vessel sealing based on temperature and electrical fields was developed. Material properties, FEM mesh, boundary conditions and solver will also be introduced in the following sections. Three FEM techniques were developed to model the three phenomena; evaporation, water loss, and tissue fusion, which occur during the sealing process.

3.3.1 Thermo-Electrical FEM Formulation

The two physics fields; temperature and electrical fields, are governed by a bio-heat transfer equation and a Laplace equation, respectively. The bio-heat transfer equation for tissue was developed in the late 1940s by Pennes (Pennes, 1948). In this study, the blood perfusion and metabolic heat sources are assumed to be negligible and the bio-heat transfer equation reduces to:

$$\rho c \frac{\partial T}{\partial t} = k \nabla^2 T + q_g \tag{3.1}$$

where ρ is the tissue density (kg/m^3), c is the tissue heat capacity (J/kg·K), t is the time (s), k is the tissue thermal conductivity (W/m·K), T is the local tissue temperature (K), and q_g is the heat generation (W) due to the externally induced electro-surgical heating of the tissue.

The electrical field in the tissue and electrode was obtained by solving the Laplace equation (Tungjitkusolmun *et al.*, 2002):

$$\nabla(\sigma\nabla V) = 0 \tag{3.2}$$

where σ is the temperature-dependent electrical conductivity (S/m) and V is the voltage (V). At the frequency range of electrosurgery, capacitive coupling in tissue is negligible and only the resistive dissipation of the electrical energy needs to be considered [23].

These two governing equations, Eqs. (3.1) and (3.2), are coupled by the heat generation term q_g. This heat generation term is defined as:

$$q_g = \boldsymbol{J}\cdot\boldsymbol{E} \tag{3.3}$$

where $\boldsymbol{J}$ is the current density (A/m^2) and $\boldsymbol{E}$ is the electric field intensity (V/m). The · in Eq. (3.3) is a scalar product operator. COMSOL Multiphysics 4.2 (Burlington, MA) is used as the platform to solve the FEM.

3.3.2 Electrode and Blood Material Properties and Tissue Thermal Conductivity

Using proper material properties is crucial to an accurate FEM. In this thermo-electrical FEM, the required material properties for each domain are density, specific heat, thermal conductivity, and electrical conductivity. Material properties for the stainless steel electrode are considered constant throughout the sealing process and are listed in Table 3.1. Due to the fluidic nature of blood and its ability to flow through and dissipate heat inside the vessel rapidly, blood material properties were assumed constant (Table 3.1). For vessel tissue, only density was assumed constant, 1050 kg/m^3. The thermal conductivity (k) of vessel tissue is assumed to be temperature-dependent and can be expressed as (Golombeck *et al.*, 1999):

$$k = k_{ref} + 0.0013(T - T_{ref}) \tag{3.4}$$

where k_{ref} (0.45 W/m·K) is the baseline tissue thermal conductivity at T_{ref} (25°C) (Duck, 1990). As the vessel tissue between the two electrodes is compressed, the water content and thermal conductivity of the tissue decrease. Therefore, a 10% reduction in the thermal conductivity was used for the tissue between the electrodes (Chastagner, 2010). The specific heat and electrical conductivity of vessel tissue change dramatically during the vessel sealing process and will be discussed in Section D along with the three FEM techniques.

Table 3.1 Material properties used in the FEM

Domain	ρ [kg/m^3]	c [J/kg·K]	k [W/m·K]	σ [S/m]
Vessel Tissue	1050*	Eq. (3.6)	Eq. (3.4)	Eq. (3.7)
Blood	1060**	3890**	0.53*	0.67***
Electrode	8000	500	16.2	$1.39 \cdot 10^6$

*Duck (Duck, 1990), **Golombeck et al. (Golombeck *et al.*, 1999) and ***Tungjitkusolmun et al. (Tungjitkusolmun *et al.*, 2002)

3.3.3 FEM Mesh, Boundary Conditions, and Solver

The configuration of the model, as shown in Figure 3.2(a), depicts the sealing of a 3 mm diameter femoral artery with a 0.4 mm wall thickness using the 5 mm Gyrus ACMI bipolar forceps from the experiment (Figure 3.1(b)). Prior research has shown that the flat contact surface accurately represents the jagged contact surface of the electrode to model the tissue temperature in electrosurgical cauterizing (Dodde *et al.*, 2008). Two planes, marked as Planes A and B, define the region to be analyzed by FEM. Plane A is across the center axis of the vessel while Plane B is the middle plane bisecting the looped electrode. On the right of Plane B, the vessel is circular with blood inside. On the left of Plane B, the vessel expands to 4.5 mm width due to the compression thermistor and fixture. It is assumed that the effect of heat transfer across Plane B is minimal and the FEM model can be simplified to the region highlighted in Figure 3.2(a). A detailed view

of the vessel and electrodes in this region is illustrated in Figure 3.2(b). The three thermistors indicate the temperature measurement points.

The cross-sectional view and detail geometry on Planes A and B are shown in Figure 3.3(a) and (b), respectively. In Figure 3.3(a), the three measurement points are shown to be 1.0, 2.0, and 3.0 mm away from the edge of the electrode. Due to the compression of the thermistors and test fixture, it was assumed that no blood was present in the first 3.0 mm from the electrode and the height of vessel tissue was 0.8 mm. For distances of 3.0 to 8.0 mm away from the electrode, without the compression of the thermistors, blood was present within the vessel, but the height of vessel remained at 0.8 mm, twice of the vessel wall thickness, due to restraint by the fixture. The wall thickness was reduced to 0.25 mm

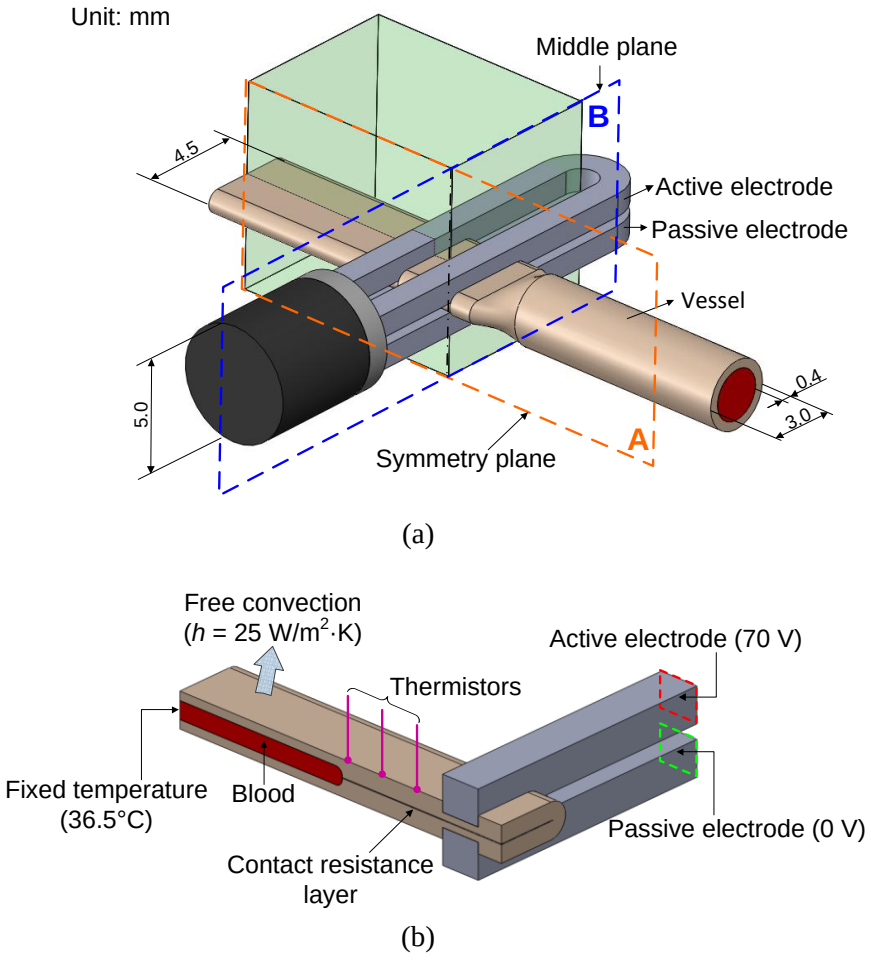

Figure 3.2 (a) Configuration of modeled vessel sealing process and (b) simplified configuration by the symmetry planes A and B and boundary conditions in the

because the present of blood flow. The vessel tissue between the electrode and Plane B had a width of 0.75 mm and a height of 0.8 mm. The height of vessel tissue between the electrodes was 0.4 mm due to the compression of the electrode. The CR layer, which will be introduced in the next section, has a thickness of 0.02 mm and extends from Plane B to 3 mm away from the electrode. As shown in Figure 3.3(b), the width of the CR layer is 1.7 mm, while one half of the compressed vessel has a width of 2.25 mm. The side of the vessel has a round fillet with 0.4 mm radius. The height of the electrode is 1.0 mm.

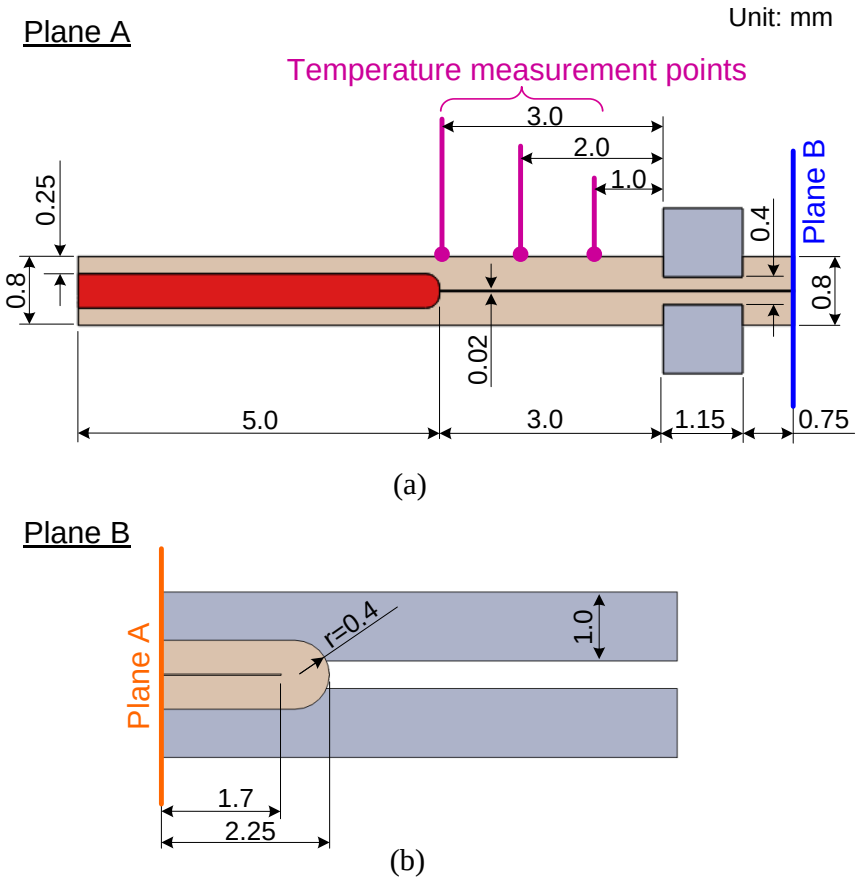

Figure 3.3 Cross-sectional view and geometry of the model on (a) symmetry Plane A and (b) symmetry Plane B

The automatic meshing generator within COMSOL was used to generate the finite element mesh. The mesh was refined until the maximum temperature at a location 1 mm from the edge of electrode differed by less than 0.2°C when compared with a finer mesh. The final mesh consisted of 30,022 linear tetrahedral elements.

For the electrical boundary conditions, an electrical insulating boundary condition was applied to all outer surfaces of the model, assuming that no electrical current flow through air and there is no electrical potential difference across Planes A and B. The experimentally measured electrical AC voltage of each pulse was first converted to a DC source voltage by calculating its root-mean-square value (Berjano, 2006) and then applied to the end surface of the active electrode. This quasi-static approximation allows for a faster time stepping and shorter computational time. Figure 3.4 shows the measured voltage and voltage input on the active electrode for FEM during the first 6 s. During the first three pulses, the FEM input voltage was 55, 65, 65 V, respectively as the voltage had not yet reached a steady level. However, after the third pulse, all subsequent pulses had a voltage input of 70 V. Each pulse has a 0.25 s on-time and 0.5 s off-time. The electrical pulses were applied for 15 s. On the passive electrode, a ground, 0 V, was applied to the end surface of the electrode. Electrical continuity was applied to all of the internal surfaces between the tissue, the blood, and the electrodes.

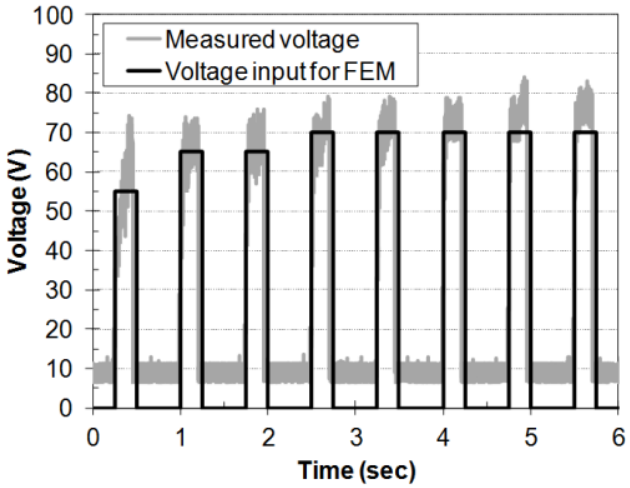

Figure 3.4 Measured voltage and voltage input for the FEM

For the thermal boundary conditions, Planes A and B were modeled as insulation surfaces with no heat flux, assuming the temperature across these planes is equal. The distal end of the blood vessel was set at 36.5°C, the body temperature of the porcine model. All the outer surfaces, except for the end of the vessel and the two symmetry planes, were subject to free convection with ambient temperature and convective heat transfer coefficient set to 25 $W/m^2 \cdot K$, respectively. Thermal continuity was applied to all

of the internal surfaces between the tissue, blood, and electrodes. The heat source (q_g in Eq. (3.3)) of total power generation from the electrical field was applied to all domains as the thermal input. The COMSOL PARDISO solver, using a stationary time iterative stepping process to solve Eqs. (3.1) and (3.2) simultaneously, was used in this study (Shenk and Gärtner, 2004). A personal computer with six cores (3.2 GHz) was used to perform the computational work. The computational time took 10 to 12 hours.

3.3.4 Three FEM Techniques to Model: Evaporation, Water Loss, and Tissue Fusion

The three physical phenomena of evaporation, water loss, and tissue fusion were modeled by the following FEM techniques. These techniques are key to accurately model the vessel sealing process and their effects will be discussed in Section V.

1) Technique 1 – Evaporation and Specific Heat:

During vessel sealing, the temperature near the electrodes is above the evaporation temperature of water. Tissue consists of about 70% water and 30% fiber (Duck, 1990). The latent heat of water, which is the energy required to evaporate from liquid to gas phase, is more than five times of the energy needed to increase the temperature from the room temperature to the evaporation temperature. The accumulation of latent heat acts as a heat sink when the tissue reaches the evaporation temperature. It is important to model the effect of latent heat due to evaporation or phase change.

The evaporation is taken into account in the FEM by varying the specific heat of tissue. The effective specific heat, c_{eff}, which varies with temperature and involves the effect of evaporation, is expressed as:

$$c_{eff} = c_f + c_w + c_l \tag{3.5}$$

where c_f is the specific heat of tissue fiber, c_w is the specific heat of water based on the water content at the corresponding temperature, and c_l is due to the latent heat of the corresponding water loss. At 25°C, c_{eff} is 3314.2 J/kg·K (Duck, 1990), c_w is 2926.9 J/kg·K (4181.3·70%), and c_l is 0, and thus c_f can be obtained to be 387.3 J/kg·K. In this

study, c_f is set as a constant. Due to the short time scales seen during vessel sealing procedures, it is assumed that all the water loss is due to evaporation and requires the accumulation of latent heat. It has been shown that the tissue water content varies with temperature (Yang *et al.*, 2007b); so that c_w and c_l can be calculated accordingly. Based on the water content at a specific temperature, the water loss as a function of temperature can be obtained.

For temperatures equal to or lower than 103°C, the equation given by Yang et al. (Yang *et al.*, 2007a) is used to calculate the percentage of water content in tissue. For temperatures higher than 103°C, the water content of temperature (W) is assumed to continue decreasing to 0.1%. W can be expressed as:

$$W = \frac{1.166}{1+e^{0.417(T-103)}}70\% + 0.1\% \tag{3.6}$$

Eq. (3.6) maintains the continuity of W at 103°C. c_w is calculated by multiplying W with the specific heat of water (4.18 J/g·K). Thus, the loss of water has an effect of reducing the specific heat. To calculate c_l, the water content with temperature is converted to a water loss function, as shown in Figure 3.5. c_l is the gradient of water loss times the latent heat of water (2260 kJ/g). By combing c_f, c_w, and c_l, c_{eff} can be calculated. The c_{eff} vs. temperature used in this study is also shown in Figure 3.5.

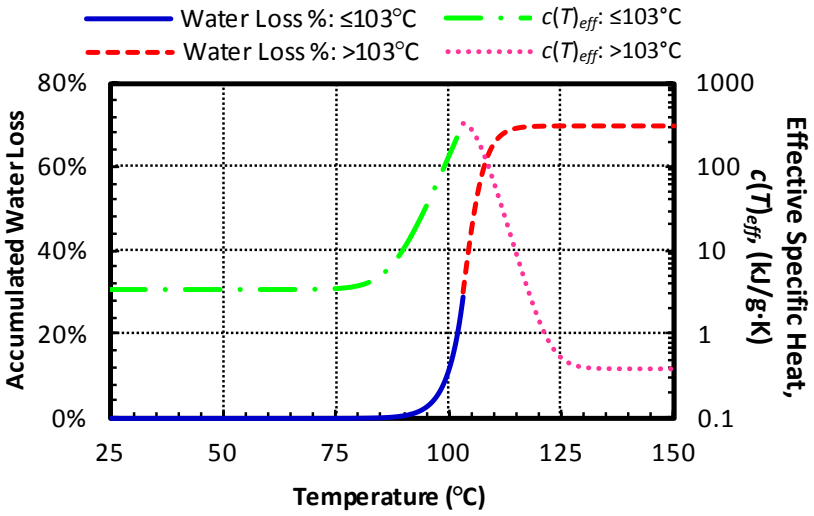

Figure 3.5 Water loss function (Yang et al., 2007b) and effective specific heat with temperature

2) Technique 2 − Water Loss and Electrical Conductivity:

During bipolar electrosurgery, the elevated tissue temperature causes evaporation that reduces the tissue water content and thus the thermally damaged tissue becomes less electrically conductive. Haemmerich et al. (Haemmerich *et al.*, 2003) used a drastic reduction in the tissue electrical conductivity (σ) of 10,000 times to define the effect of thermal damage on σ. This reduction in σ is caused by the loss of water in the tissue as water is the primary carrier medium for the electrical current in the tissue. Thus, the water loss causes the σ of the tissue to fall. In this study, when T<103°C, the σ was assumed to increase at a rate of 2%/°C (Berjano, 2006) and can be expressed as:

$$\sigma = \sigma_{ref}\left[1+0.02(T-T_{ref})\right] \tag{3.7}$$

where σ_{ref} is the reference electrical conductivity of the tissue (0.55 S/m (Duck, 1990)) and T_{ref} is the reference temperature (25°C).

Once the tissue accumulated enough energy for the phase changing process, meaning the loss of water, the σ was set at a low, constant value, designated as σ_d. In this study σ_d = 0.01 S/m. The σ with thermal damage is denoted as σ'. The transition between σ and σ_d is smoothed to be continuous with their first derivative by COMSOL.

3) Technique 3 − Tissue Fusion and Electrical CR:

Electrical CR exists at the interface of two conductive surfaces and is well studied for industrial spot welding processes (Li, 2005). In vessel sealing, the electrical CR also exists between the contact surfaces inside the vessel and is important for accurate prediction of temperature.

At 25°C, the CR for an area of 50 mm was experimentally determined to have resistance ranging from 123 to 243 Ω with the bioimpedance measurement system developed by Dodde et al. (Dodde et al., 2012). In vessel sealing, the vessel is compressed by the electrode, forcing the contact of vessel wall inner surface. Once the tissue is heated, the proteins in tissue unwind and realign to form a fused region, which seals the vessel (Wright and Humphrey, 2002). The fusion process starts at 70−80°C (Wu *et al.*, 2000). Once the vessel wall is fused together, the CR is removed.

In this study, to simulate the process of tissue fusion, a thin (0.02 mm) CR layer was initially added to the interface where the vessel walls were compressed and touched each other. The electrical conductivity of the CR layer (σ_{CR}) is equal to 0.005 S/m for temperatures below 80°C. For temperatures above 90°C, meaning the fusion process has completed, the CR layer is removed by changing σ_{CR} to the same value as the vessel tissue (σ') at the corresponding temperature. For 80−90°C, σ_{CR} linearly transitions from 0.005 S/m to σ'.

Based on the change in electrical conductivity due to water loss and the removal of the CR layer, the sealing process can be divided into three phases, as shown in Figure 3.6. In Phase 1, the pathway with the least electrical resistance is passing along the vessel wall between two electrodes but not going through the CR layer. The current flow causes resistive heating to concentrate in this region and the local thermal damage can be seen quickly. This thermally damaged region has a reduced electrical conductivity; therefore, the current stops passing through this region and spreads out to the tissue away from the edge of electrodes. This phenomenon causes the resistive heating to spread to a wider area. When all the tissue adjacent to the edge of electrode is thermally damaged and has reduced electrical conductivity, it once again creates a barrier to prevent current from spreading out. This is the start of Phase 3. At this time, the temperature of CR layer between the electrodes has exceeded 90°C and the electrical conductivity is changed to σ'. In Phase 3, the current is constrained only in the region between the two electrodes and has a minimal resistive heating effect for tissue away from the electrode.

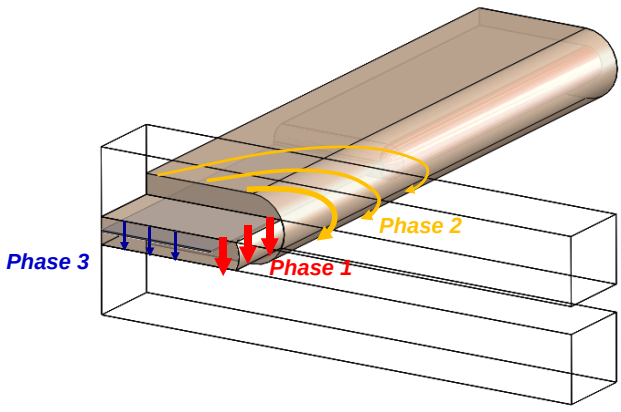

Figure 3.6 Schematic of current path in each phase (vessel tissue between the electrode and Plane B is not shown)

3.4 Experimental Results and Validation of FEM

3.4.1 Experimental Results

Figure 3.7 shows the comparison of experimentally measured tissue temperature with the FEM predictions during electrosurgical vessel sealing. The temperatures at the three points, 1.0, 2.0, and 3.0 mm away from the bipolar electrode (Figure 3.4(a)) are presented. The result of each phase is described separately as follows.

1) Phase 1 − Pre-fusion:

The temperature at 1.0 mm increased slowly during the first 1.5 s. The temperature at 2.0 and 3.0 mm did not increase much in this phase. Since most of the electrical current went laterally along the vessel wall, the local tissue in this region was thermally damaged and the effect of tissue fusion was limited.

2) Phase 2 − Fusion:

Both the temperatures at 1.0 and 2.0 mm increased rapidly during Phase 2 (1.5−4.3 s). The CR forces more electrical current to spread out and causes the resistive heating of tissue at 1.0 and 2.0 mm adjacent to the electrode. The rapid temperature increase at 1.0 and 2.0 mm indicates the existence of resistive heating. The wider current distribution due to the CR layer also forces some electrical current to pass through this layer. The current passing through the CR layer heats up the interface of vessel wall to achieve the effect of tissue fusion. Thus, most of the tissue fusion which forms the vessel seal happens during Phase 2. If the electrical energy stops before Phase 2 is finished, the seal may not have enough strength because only a limited area is fused. This inference agrees with what Dilley et al. (Dilley *et al.*, 1995) have suggested that a sufficient sealing time is required to form a strong seal. Phase 2 ends at 4.3 s in this study which is also close to the sealing time (2.06−4.5 s) used by Newcomb et al. (Newcomb *et al.*, 2009). At the end of Phase 2, the temperature at 1.0 mm reached a maximum value of 80.8°C. The temperature at 3.0 mm started increasing gradually from Phase 2. The gradual increase indicates that the temperature change can be attributed to heat conduction.

3) Phase 3 − Post-fusion:

In this phase (4.3-15 s), temperatures between the two electrodes exceeded the tissue denature temperature (90°C), the tissue had fused, and the CR layer was removed.

Thus, the electrical current was restrained between the two electrodes thereafter. There is no resistive heating away from the electrode. This explains why the temperature remained at the same level after 4.3 s even with continuing generator activation. As a result, the temperature at 1.0 mm decreased slowly to 74°C, even as electrical pulses were continued. At 2.0 mm, the temperature remained relatively steady and only increased by 4°C during this phase. At 3.0 mm, the temperature continued increasing through the entire phase by 16°C.

3.4.2 Validation of FEM

As shown in Figure 3.7, the FEM accurately predicts general trends for thermal profiles during the electrosurgical vessel sealing compared to the experimental measurements. The average error is 6.9% and the standard deviation of error is 4.2%. The overall maximum error is 23.9%. At 1.0 mm, the temperature increases during the first two pulses is slightly higher than that in the experiment. The model reaches the maximum temperature at the same time (4.3 s) as in the experiment and the predicted value is 0.8°C higher. The average errors in Phases 1 and 2 are 11.3% and 7.2%, respectively. The maximum error (23.9%) happens at around 1.5 s, which is at the end of Phase 1. Two reasons may contribute to the higher error rate in Phase 1. First, a delay of the temperature measurement is caused by the time constant of the thermistor (250 ms). Second, the early temperature increase in the model might be the result of not modeling the tissue fluid movement due to compression. Tissue compression expels the water from the tissue being compressed to the adjacent tissue. In the experiment, the electrical current would concentrate in the tissue with more water, and therefore a higher electrical conductivity. On the other hand, the model shows a higher saturated temperature in the Phase 3. A possible reason is that the thermistor fixture was not modeled in the FEM. This fixture may absorb some thermal energy and lower the tissue temperature.

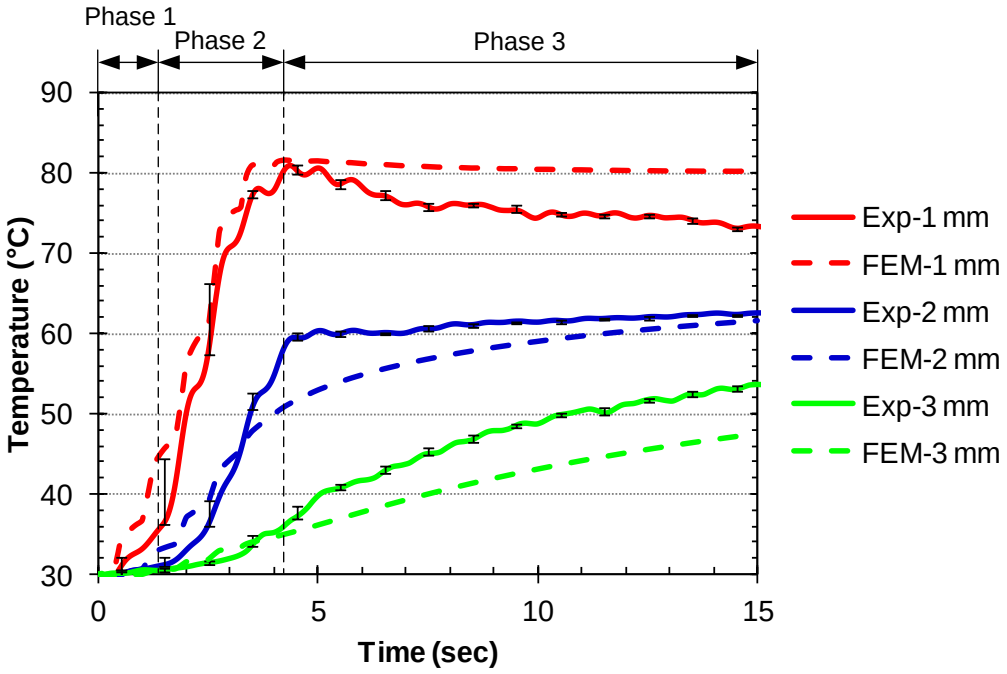

Figure 3.7 Comparison of Experimental, 3D FEM temperature profiles (the error bars show the temperature change within the time constant of the thermistor ± the tolerance of the thermistor)

At 2.0 mm, the temperature generally matches the experimental results. The average errors for Phases 1, 2, and 3 are 1.9%, 8.1%, and 4.9%, respectively. The maximum error (13.5%) occurs in Phase 2. The predicted temperature increases slightly slower than in the experiment, which causes the larger error. This is attributed to the mass transfer that occurs due to the water vaporization as it carries the heat away from the heating region (Ward *et al.*, 2007). This mass transfer effect is not included in this study because the model has predicted the temperature reasonably well without considering the mass transfer. It is expected that the heated water vapor moves from the high tissue temperature regions to surrounding low temperature regions. The vapor carries heat away and condensates in the lower temperature regions.

At 3.0 mm, the FEM result underestimates temperature. The temperature increase at this position is mostly due to heat conduction. Since the temperature predicted at 2.0 mm is lower than the experiment (at the beginning of Phase 3), it is expected that the temperature at 3.0 mm will also be lower. The average errors for Phases 1, 2, and 3 are 1.0%, 2.2%, and 11.0%, respectively. The maximum error 12.4% is found in Phase 3.

3.5 Investigation of the Effects of FEM Techniques

In this section, the effects of the three FEM techniques on the temperature profiles are presented and discussed.

3.5.1 Effect of Specific Heat (Technique 1)

The temperature profiles of a model without Techniques 1 (c_{eff}) and 2 (σ') is compared to a model with Techniques 1 and 2, and another model with Technique 1 only in Figure 3.8. The temperature at 0.8 mm away from the electrode is presented for illustration purposes because the FEM techniques are more pronounced at this point. In the model without both Techniques 1 and 2 (shown in solid-dot line), the temperature keeps increasing. As Technique 1 is incorporated (dashed line), the rate of temperature increase is slowed as the temperature approaches the evaporation point. The slower increasing rate indicates the accumulation of latent heat as water is vaporized. This effect can also be seen in Figure 3.9 (dashed line, 0.2-0.4 mm). Once most of the water is evaporated (at 11 s), there is only tissue fiber left and c_{eff} drops close to c_f. Thus, the temperature increases rapidly. It also shows a larger temperature oscillation with the on and off of the electrical pulses input because of the low specific heat. The temperature then continues increasing to over 200°C till the end of the measurement.

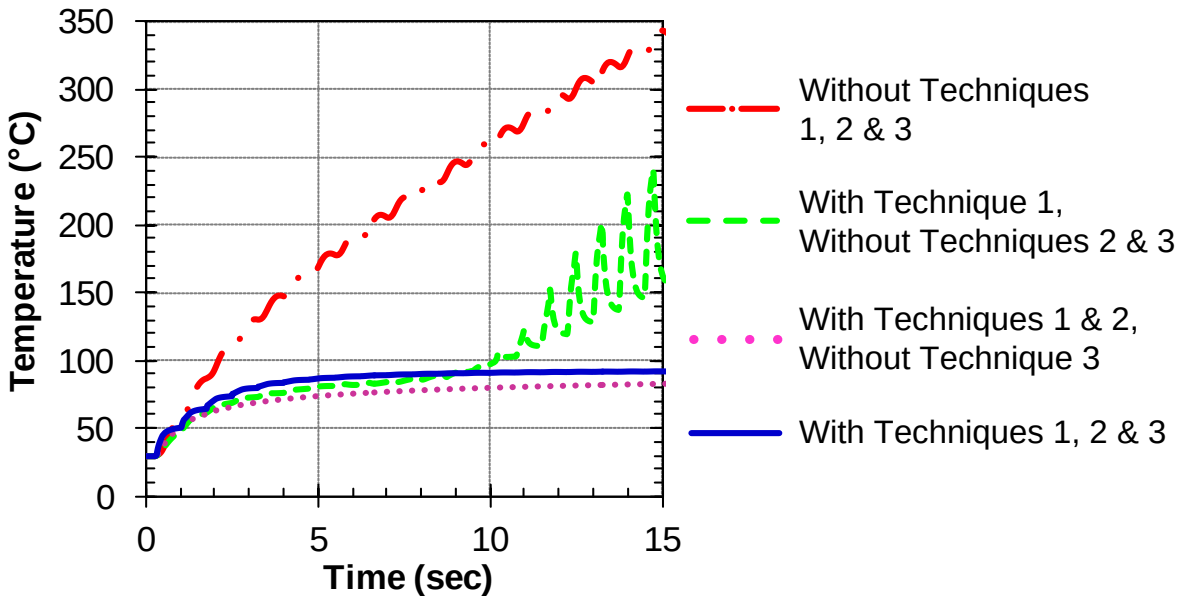

Figure 3.8 . Effects of Techniques 1 and 2 showing temperature profiles at 0.8 mm away from the edge of electrode

3.5.2 Effect of Water Loss on Electrical Conductivity (Technique 2)

The effect of thermal damage on electrical conductivity can also be illustrated by Figure 3.8. The dotted line shows the temperature result of a model with both Techniques 1 and 2 incorporated. Compared to the model with Technique 1 but without Technique 2 (dashed line), the temperature remains below the evaporation point. This is because, with the onset of thermal damage, the electrical conductivity is lowered to 0.01 S/m once the water is evaporated. Such low electrical conductivity attenuates the resistive heating. Without considering the effect of water loss due to evaporation on electrical conductivity, the vessel tissue remains conductive at high temperature and thus allows resistive heating that causes temperature increase.

3.5.3 Effect of Tissue Fusion and CR (Technique 3)

Figure 3.9 shows the spatial temperature profiles at 4.3 s along the thermistors locations from the edge of the electrode. . The temperature profiles between the results from model with and without Technique 3 (solid and dotted line, respectively) is 20°C at 1 mm and 15°C at 2 mm. The existence of the CR layer effectively forces the electrical current to spread out to a wider area and thus causes more resistive heating in areas further away from the electrode.

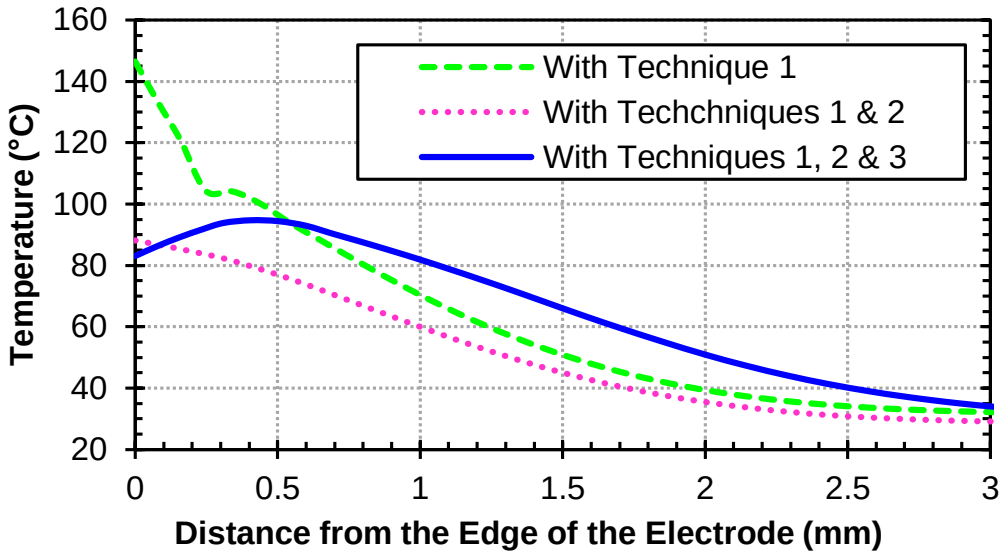

Figure 3.9 Spatial temperature profile along the thermistor positions at 4.3 s

3.6 Conclusions

This study presented an advanced bio-heat transfer FEM with three techniques that were critical to enable the accurate prediction of the temporal and spatial distributions of tissue temperature during electrosurgical vessel sealing. This FEM has been experimentally validated by an *in-vivo* porcine femoral artery model. With the FEM techniques developed in this study, the accuracy of FEM for electrosurgical vessel sealing has been improved significantly and demonstrated the importance of incorporating the effective specific heat accounting for latent heat, the effect of water loss on electrical conductivity, and the CR for tissue fusion.

Two future research directions have been identified. One is a more comprehensive study on CR and tissue fusion in electrosurgical vessel sealing. An estimated conductivity (0.005 S/m) of the CR layer was used and the regions of progressive change of CR were designated. The other is the effect of mass transfer, particularly the water in the tissue. The movement of tissue fluid due to compression and vaporization needs to be further studied. The water content of tissue has significant effects on tissue thermal and electrical conductivity. The coupled effect of mass and bio-heat transfer will be studied to further improve the accuracy of the FEM prediction.

References

Berjano E J 2006 Theoretical modeling for radiofrequency ablation: state-of-the-art and challenges for the future *Biomedical Engineering Online* **5** 24

Campagnacci R, de Sanctis A, Baldarelli M, Rimini M, Lezoche G and Guerrieri M 2007 Electrothermal bipolar vessel sealing device vs. ultrasonic coagulating shears in laparoscopic colectomies: a comparative study *Surg. Endosc.* **21** 1526-31

Campbell P A, Cresswell A B, Frank T G and Cuschieri A 2003 Real-time thermography during energized vessel sealing and dissection *Surg. Endosc.* **17** 1640-5

Chastagner M W 2010 Invesitgation of eletrosurgical tissue joining. In: *Mech. Eng.*, (Ann Arbor: University of Michigan-Ann Arbor)

Dewhirst M, Viglianti B, Lora-Michiels M, Hanson M and Hoopes P 2003 Basic principles of thermal dosimetry and thermal thresholds for tissue damage from hyperthermia *Int. J. Hyperthermia* **19** 267-94

Dilley A V, Mary-Anne G F and David L M 1995 An experimental study of optimal parameters for bipolar electrocoagulation *Gastrointest. Endosc.* **42** 27-30

Dodde R E, Bull J L and Shih A J 2012 Bioimpedance of soft tissue under compression *Physiol. Meas.* **3** 1095-109

Dodde R E, Miller S F, Geiger J D and Shih A J 2008 Thermal-electric finite element analysis and experimental validation of bipolar electrosurgical cautery *Journal of Manufacturing Science and Engineering* **130** 021015-1-8

Duck F A 1990 *Physical properties of tissue: a comprehensive reference* (London: Academic Press)

Goldberg S N 2001 Radiofrequency tumor ablation: principles and techniques *Eur. J. Ultrasound* **13** 129-47

Golombeck M A, Dossel O, Saubert A and Tonnier V M 1999 Magnetic resonance imaging with implanted neurostimulators: a first numerical approach using finite integration theory. In: *International Symposium on Electromagnetic Compatibility*, (Magdeburg, Germany

Haemmerich D, Chachati L, Wright A S, Mahvi D M, Lee F T, Jr. and Webster J G 2003 Hepatic radiofrequency ablation with internally cooled probes: effect of coolant temperature on lesion size *IEEE Trans. Biomed. Eng.* **50** 493-500

Heniford B, Matthews B, Sing R, Backus C, Pratt B and Greene F 2001 Initial results with an electrothermal bipolar vessel sealer *Surg. Endosc.* **15** 799-801

Kennedy J S, Stranahan P L, Taylor K D and Chandler J G 1998 High-burst-strength, feedback-controlled bipolar vessel sealing *Surg. Endosc.* **12** 876-8

Li W 2005 Modeling and on-line estimation of electrode wear in resistance spot welding *J. Manuf. Sci. Eng.* **127** 709-17

Martin G T and Angelone L 2009 Multiphysics model of the NovaSure endometrial ablation procedure. In: *The COMSOL Conference*, (Boston, MA

Newcomb W, Hope W, Schmelzer T, Heath J, Norton H, Lincourt A, Heniford B and Iannitti D 2009 Comparison of blood vessel sealing among new electrosurgical and ultrasonic devices *Surg. Endosc.* **23** 90-6

Pearce J A and Thomsen S L 1992 Kinetic models of tissue fusion processes. In: *Proc. of SPIE 1643*, pp 251-5

Pennes H H 1948 Analysis of tissue and arterial blood temperatures in the resting human forearm *J. Appl. Physiol.* **1** 93-122

Ponsky T A, Khosla A and Rothenberg S S 2009 Experience with a new energy source for tissue fusion in pediatric patients *J. Laparoendosc. Adv. Surg. Tech.* **19** 1-3

Shen W T, Baumbusch M A, Kebebew E and Duh Q Y 2005 Use of the electrothermal vessel sealing system versus standard vessel ligation in thyroidectomy *Asian J. Surg.* **28** 86-9

Smaldone M C, Gibbons E P and Jackman S V 2008 Laparoscopic nephrectomy using the EnSeal tissue sealing and hemostasis system: successful therapeutic application of nanotechnology *JSLS* **12** 213-6

Tungjitkusolmun S, Staelin S T, Haemmerich D, Tsai J Z, Cao H, Webster J G, Lee Jr F T, Mahvi D M and Vorperian V R 2002 Three-dimensional finite-element analyses for radio-frequency hepatic tumor ablation *IEEE Trans. Biomed. Eng.* **49** 3-9

Tungjitkusolmun S, Woo E J, Cao H, Tsai J Z, Vorperian V R and Webster J G 2000 Thermal-electrical finite element modelling for radio frequency cardiac ablation: effects of changes in myocardial properties *Med Biol Eng Comput* **38** 562-8

Vellimana A K, Sciubba D M, Noggle J C and Jallo G I 2009 Current technological advances of bipolar coagulation *Neurosurgery* **64** 11-9

Ward A K, Ladtkow C M and Collins G J 2007 Material removal mechanisms in monopolar electrosurgery. In: *29th Annual International Conference of the IEEE* (Lyon, France pp 1180-3

Wright N T and Humphrey J D 2002 Denaturation of collagen via heating: an irreversible rate process *Annu Rev Biomed Eng* **4** 109-28

Wu M P, Ou C S, Chen S L, Yen E Y and Rowbotham R 2000 Complications and recommended practices for electrosurgery in laparoscopy *Am. J. Surg.* **179** 67-73

Yang D, Converse M C, Mahvi D M and Webster J G 2007a Expanding the bioheat equation to include tissue internal water evaporation during heating *IEEE Trans. Biomed. Eng.* **54** 1382-8

Yang D, Converse M C, Mahvi D M and Webster J G 2007b Measurement and analysis of tissue temperature during microwave liver ablation *IEEE Trans. Biomed. Eng.* **54** 150-5

CHAPTER 4
THERMO-ELECTRICAL MODELING OF BIPOLAR COAGULATION ON POSTERIOR SPINAL ARTERY IN A PORCINE SPINAL SURGERY MODEL

ABSTRACT

A thermo-electrical model, with both solid and liquid phases to calculate tissue temperature during bipolar coagulation of a posterior spinal artery on the spinal cord is developed. Control of thermal spread caused by coagulation is a concern in spinal surgery as neural tissues are vulnerable to thermal injury. When the electrical energy is applied, the spinal fluid on top of spinal cord flows due to electrical field and thermal convection. The flow of the spinal fluid affects the temperature distribution because the heat may be carried away by the fluid flow. The model developed in this study incorporates the flow effect to accurately predict the temperature profiles. The model is validated by ex-vivo temperature measurements on a porcine spinal cord model. The maximum error on tissue temperature of this model is 12.6% and the overall average error is 4.2%. The lesion region (>50ºC) is identified and thermal dose, cumulative equivalent minutes at 43°C (CEM43), is also calculated with this model.

Contents of this chapter will be submitted to *IEEE Transaction on Biomedical Engineering* as Roland K. Chen, Khoi D. Than, Paul Park, and Albert J. Shih, "Thermo-Electrical Modeling of Bipolar Coagulation on Posterior Spinal Artery in a Porcine Spinal Surgery Model."

4.1 Introduction

Bipolar coagulation is an important procedure to control bleeding in neurosurgery. This procedure involves the use of electrical energy to generate heat in both spinal cord or brain (solid phase) and cerebrospinal fluid (liquid phase). The concept of bipolar forceps was first presented by Greenwood in 1940 (Greenwood Jr, 1940) and remains a standard configuration to this day. The first commercial bipolar coagulation system was developed by Malis (Malis, 1967) in the 1960s. This bipolar approach of delivering electrical current to tissue successfully restrains the electrical energy and joule heating in a smaller volume of tissue, comparing to that of the monopolar manner (Chehrazi and Collins Jr, 1981). The thermal spread due to the coagulation may introduce thermal injury to the surrounding neural tissue and lead to undesirable surgical outcomes.

In neurosurgery, bipolar forceps with sharp tips (0.25 mm to 2 mm wide) are used in delicate surgical procedures (often performed under microscopic visualization) to coagulate vessels right on the surface of the spinal cord or cerebral cortex, which have a low temperature threshold for thermal injury (around 43°C) (Dewhirst *et al.,* 2003). Different coatings on the tip, such as silver and gold, have been used to help dissipate heat and prevent tissue sticking (Mikami *et al.,* 2004). Heat pipe has also been incorporated into the bipolar forceps (Elliott-Lewis *et al.*, 2010; Elliott-Lewis *et al.,* 2009; Arakawa, 2005) and shown to reduce thermal damage compared to conventional forceps. Since the tissue must be heated to seal the vessel, the adjacent tissue is at risk of thermal damage because of the thermal spread from the sealing site.

A better understanding of the thermal spread can help to prevent and reduce the thermal injury in neurosurgery. The temperature distribution in the tissue is difficult to quantify. Even with an infrared thermal camera, only the surface temperature can be measured. The subsurface thermal injury information relies on histological analysis which cannot determine the tissue temperature (Elliott-Lewis *et al.*, 2010). An accurate thermo-electrical finite element modeling (FEM) provides insightful information for thermal spread temporally and spatially.

Previous studies on electrosurgical modeling, combining Joule heating and bio-heat transfer, focused primarily on tumor ablation in different organs (Haemmerich *et al.*, 2003; Martin and Angelone, 2009; Tungjitkusolmun *et al.*, 2000) or vessel sealing (Chen

et al., 2012). However, all these studies only modeled the solid phase heat conduction. While in the case of vessel coagulation in neurosurgery, the cerebrospinal fluid (or its mixture with saline due to irrigation) on the surface plays an important role, not only on current dissipation but also on heat distribution.

Electrothermally induced fluid flow has been studied intensively to manipulate and separate bioparticles (Green *et al.*, 2001; Ramos *et al.*, 1999b; Green *et al.*, 2000). When electrical current is applied to a conductive fluid (for example, the NaCl solution), the electrical field will generate the electrical force not only on the particles but also on the fluid (Ramos *et al.*, 1999a). In these studies, the gravity force, which varies with fluid density and is related to temperature, is neglected because the overall temperature rise is less than 20ºC. However, during the coagulation, the temperature can increase more than 70ºC and the gravity force may not be negligible.

In this study, we aim to develop a two-phase (solid-liquid) thermo-electrical FEM to predict the temporal and spatial distributions of tissue temperature during bipolar coagulation of a posterior spinal artery on the surface of spinal cord. The stainless steel bipolar forceps (0.5 mm tip radius) without any special coating are used to perform coagulation and the experiment results are used to validate the FEM. With this model, the tissue coagulation region is identified

An ex-vivo porcine animal model was used for the experiment. All the procedures were done in the animal surgery operating room at the University of Michigan Medical School compliant to the protocol approved by the University Committee on Use and Care of Animals. A stainless steel bipolar forceps (DePuy Codman & Shurtleff, Warsaw, IN) was used to perform coagulation (Figure 4.1(a)).

Tissue temperature was measured by micro-thermistors (Model: 56A1002-C8; Alpha Technics, Irvine, CA). This type of thermistor was chosen because of its small dimension (0.46 mm outside diameter) and relative immunity to electromagnetic interference (Dodde *et al.*, 2009). The thermistor has a measurement tolerance of ± 0.1°C and 250 ms thermal response time. The temperature reading was acquired by a data acquisition system (PXI-1033; National Instruments, Austin, TX) with 100 Hz sampling rate. The tissue temperature was measured at three positions: midpoint between forceps tips (thermistor #1), 1.0 mm (thermistor #2), and 2.0 mm (thermistor #3) away from the

midpoint along the centerline, as shown in Figure 4.1(a) and later in Fig. 3(a). An acrylic fixture was created to ensure temperature measurements were recorded at precise locations (Figure 4.1(c)). The spacing between the forceps tips were fixed at 2.0 mm by use of another fixture, as shown in Figure 4.1(a). The voltage and current input to the bipolar forceps were measured by a voltage probe (Model: 10076A, Agilent, Santa Clara, CA) and a current probe (Model: 1147A, Agilent), respectively. These electrical data were collected at 4 MHz.

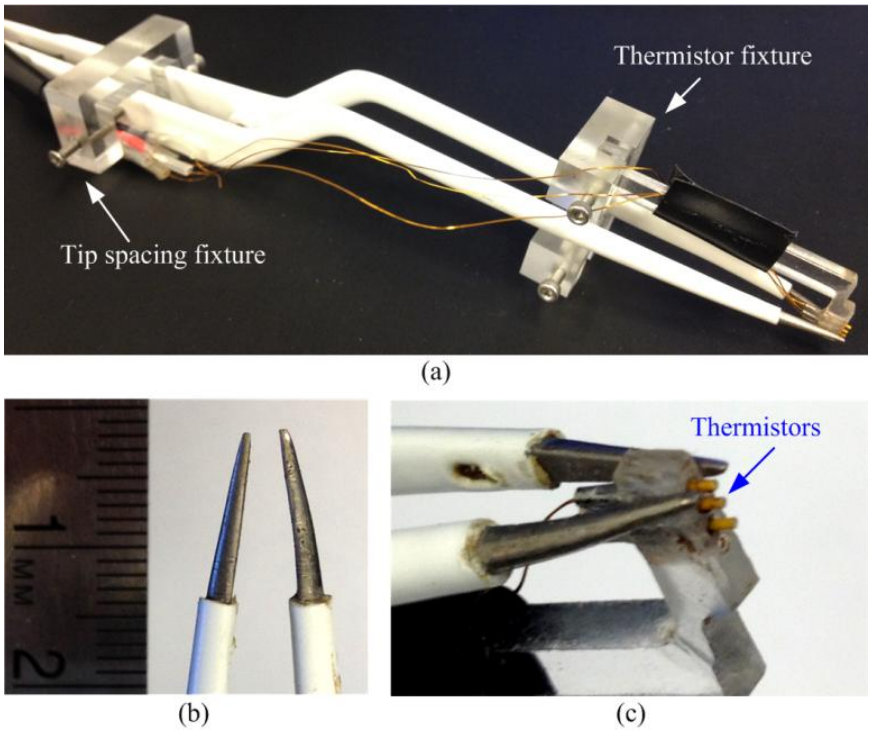

Figure 4.1 The bipolar forceps used in this study (a) overview, (b) close-up view of forceps tips, and (c) forceps tip with temperature measurement setup

The experiment was carried out immediately after the pig was euthanized. The dura mater of the porcine spine was opened by a neurosurgeon to expose a posterior spinal artery on the spinal cord, as shown in Figure 4.2(a). Two arteries with diameter of 0.4 to 0.5 mm were chosen to be coagulated. The forceps were powered by an electrosurgical generator, Valleylab Force FX (Covidien, Boulder, CO) with 25 Malis units. Activation time of the generator was fixed at 5 seconds.

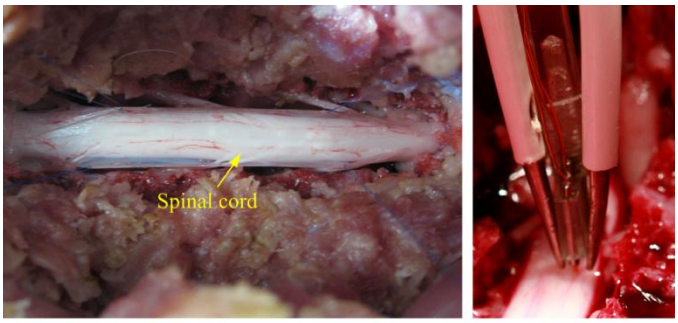

Figure 4.2 (a) Spinal cord with dura mater opened and (b) coagulation of the posterior spinal artery on spinal cord

4.2 Finite Element Modeling

The two-phase (solid-liquid) thermo-electrical FEM consists of two physics fields: thermal and electrical fields. The electrical field was governed by Laplace equation and coupled to the thermal field by a Joule heat generation term. In the thermal field, the solid and fluid phases were modeled by heat conduction in solids and non-isothermal flow, respectively. There are four dependent variables solved in the model: voltage, temperature, velocity, and pressure. The formulations for electrical field, heat conduction in solids and non-isothermal flow are introduced in the following sections.

4.2.1 Electrical Field Formulation

The electrical potential (V) in the tissue and electrode has been described in a previous study by solving the Laplace equation (Chen *et al.*, 2012). The electrical field, **E** (V/m)) can be obtained by calculating the gradient of electrical potential.

$$\mathbf{E} = -\nabla V \tag{4.1}$$

The current density, **J** (A/m^2) is then calculated by

$$\mathbf{J} = \sigma \mathbf{E} \tag{4.2}$$

where σ is the temperature-dependent electrical conductivity (S/m). The Joule heat generation term, q_g can be calculated by multiplying the electrical field with the current density and used to couple the electrical field to thermal field.

4.2.2 Thermal Field Formulation

Heat Conduction in Solid:

The general bio-heat equation for conduction in solids developed by Pennes *(Pennes, 1948)* can be expressed as:

$$\rho c \frac{\partial T}{\partial t} = k\nabla^2 T + \rho_b c_b w_b (T - T_b) + q_m + q_g \tag{4.3}$$

where ρ is the tissue density (kg/m^3), c is the tissue heat capacity (J/kg·K), t is the time (s), k is the tissue thermal conductivity (W/m·K), T is the local tissue temperature (K), ρ_b is the blood density (kg/m^3), c_b is the blood heat capacity (J/kg·K), w_b is the effective blood perfusion parameter (1/s), T_b is the blood temperature (K), q_m is the metabolic heat generation rate (W/m^3), and q_g is the heat generation (W/m^3) due to the externally induced electrosurgical heating of the tissue. In the *ex-vivo* case, it is assumed that the metabolic heat generation and blood perfusion were zero (q_m = 0 and w_b = 0).

Non-isothermal Flow:

Given that metabolic heat generation and blood perfusion were zero, the heat transfer equation for a non-isothermal flow can be simplified as *(Kraus* et al.*, 2012)*:

$$\rho c \frac{\partial T}{\partial t} + \rho c \mathbf{u} \cdot \nabla T = k\nabla^2 T + q_g \tag{4.4}$$

where **u** is the velocity field of the fluid (m/s). The velocity for a Newtonian incompressible fluid is governed by Navier-Stoke's equation (Gonzalez *et al.*, 2000):

$$\rho \frac{\partial \mathbf{u}}{\partial t} + \rho \mathbf{u} \cdot \nabla \mathbf{u} = -\nabla p + \mu \nabla^2 \mathbf{u} + \mathbf{F}_e + \mathbf{F}_g \tag{4.5}$$

and the continuity equation:

$$\frac{\partial \rho}{\partial t} + \nabla \cdot (\rho \mathbf{u}) = 0 \tag{4.6}$$

where p is the pressure (N/m^2), μ is the viscosity of spinal fluid (kg/m·s), $\mathbf{F}_e$ is the electric force density (N/m^3) and $\mathbf{F}_g$ is the volume force caused by gravity (N/m^3). The electrical force density is estimated by (Green *et al.*, 2001):

$$\mathbf{F}_e = \rho_q \mathbf{E} - \frac{1}{2} E^2 \nabla \varepsilon \tag{4.7}$$

where ρ_q is the charge density, and E is the magnitude of the electrostatic field, and ε is the permittivity (Gabriel *et al.*, 1999). The gravity force is:

$$\mathbf{F}_g = \rho \mathbf{g} \tag{4.8}$$

where g is the gravity, 9.8 m/s^2.

4.2.3 Material Properties

Materials modeled in this two-phase thermo-electrical FEM include the spinal cord, artery wall, spinal fluid, blood, and stainless steel (for bipolar forceps) and thermistor. Table 4.1 lists the density (ρ), specific heat (c), thermal conductivity (k), electrical conductivity (σ), and viscosity (μ).

The density of spinal fluid is considered as temperature-dependent and is given by Arps (Arps, 1953). The change of density with temperature is a nature of fluid which causes the heat convection. Specific heat of tissue has been modified to account for the accumulation of latent heat (Yang *et al.*, 2007). In this study, the effective specific heat which is based on the water loss with temperature is used for both spinal cord and artery wall.

The thermal conductivities of spinal cord and artery wall are assumed to be temperature-dependent and can be expressed as (Golombeck *et al.*, 1999):

$$k = k_{ref} + 0.0013(T - T_{ref}) \tag{4.9}$$

where k_{ref} is the reference thermal conductivity at T_{ref} (25°C). The k_{ref} for spinal cord and artery wall are listed in Table 4.1. The electrical conductivities of spinal cord and artery

wall are also assumed to be temperature dependent, increasing at a rate of 2%/°C (Berjano, 2006), and can be expressed as:

$$\sigma = \sigma_{ref}\left[1 + 0.02(T - T_{ref})\right] \tag{4.10}$$

where σ_{ref} is the reference electrical conductivity at T_{ref} (25°C). The reference electrical conductivities for spinal cord and artery wall can be found in Table 4.1. This increasing rate is only applied for T<103°C. For T≥103°C, the tissue is considered to be thermally damaged and will have a low electrical conductivity of 0.01 S/m (Chen *et al.*, 2012).

Table 4.1 Material Properties Used in the FEM

Domain	ρ [kg/m^3]	c [J/kg·K]	k [W/m·K]	σ [S/m]	μ [Pa S]
Spinal cord	1038 [a]	3600 [a]	0.503*, [a]	0.60**, [a]	-
Artery wall	1050 [a]	3314 [a]	0.450*, [a]	0.33**, [d]	-
Spinal fluid	$\rho(T)$ [b]	3900 [a]	0.570 [a]	1.53 [a]	$7.15\cdot10^{-4}$ [f]
Blood	1060 [c]	3890 [c]	0.531 [a]	0.67 [e]	-

*Used as k_{ref} in Eq. (4.9), **used as σ_{ref} in Eq. (4.10)
a: Duck (Duck, 1990), b: Arps (Arps, 1953), c: Golombeck et al. (Golombeck *et al.*, 1999), d: Edgerton (Edgerton, 1975), e: Tungjitkusolmun et al. (Tungjitkusolmun *et al.*, 2002), and f: Brydon et al. (Brydon *et al.*, 1995)

4.2.4 Model Configuration, Mesh, Boundary Conditions, and Computational Solver

The configuration of the model is shown in Figure 4.3 with the tips of bipolar forceps across a posterior spinal artery near the surface of the spinal cord. The spinal cord is covered by a thin (0.15 mm) layer of spinal fluid. The thermistors used to measure temperature are also included in the model because the size of the thermistor is in a similar scale to other features and thus the effect of thermistor needs to be considered. The spinal cord tissue is modeled as a block with 20.0 mm long, 15.0 mm wide, and 10.0 mm thick. The first thermistor locates in the midpoint of the two tips, as shown in Figure 4.3(a). The second and third thermistors are 1.0 and 2.0 mm away from the first thermistor along the centerline, respectively. Figure 4.3(b) shows the close-up view of the

cross-sectional plane across the forceps tips and details of the geometry of the FEM. The spacing of the tips is 2.0 mm. The thermistor has a diameter of 0.46 mm and 3.0 mm long. The spinal fluid layer has a thickness of 0.15 mm. The artery is assumed to be straight throughout the block of spinal cord. The artery wall has an outside diameter of 0.5 mm and 0.4 mm inside diameter. The center of the artery is 0.3 mm below the surface of the spinal cord.

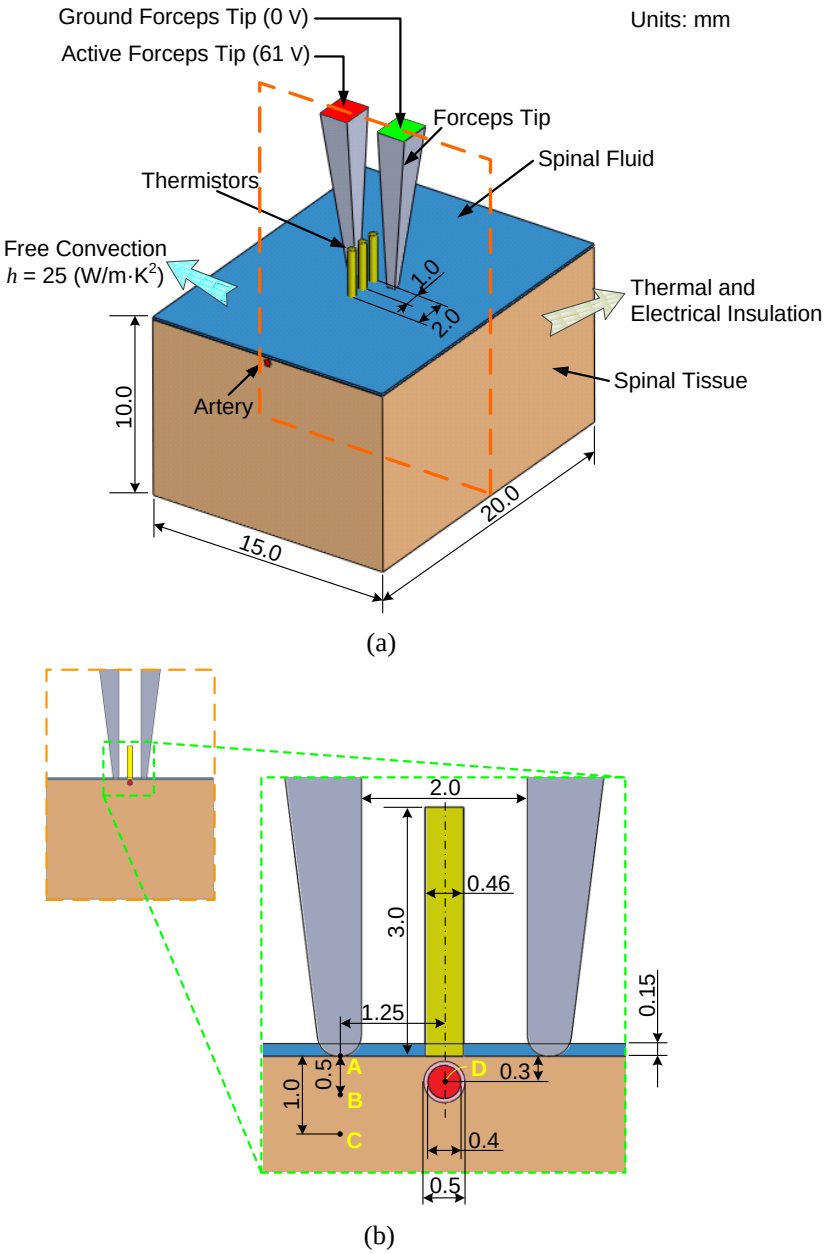

Figure 4.3 (a) Configuration of modeled bipolar coagulation on a spinal artery and (b) detailed geometry on the cross section across the forceps tips

The FEM mesh is generated based on each domain. For the spinal fluid layer, the maximum element size is 0.05 mm, so that there are at least three elements across the thickness of the fluid layer. The maximum element growth rate is 1.2 for remesh. The mesh is refined until the maximum temperature at the midpoint between forceps tips differed by less than 0.1°C compared to a finer mesh. The final mesh consisted of 353,991 tetrahedral elements and a total of 1,359,631 degree of freedoms. The velocity components were discretized by second order elements and all other dependent variables (pressure, temperature, and voltage) were by linear elements.

For the electrical boundary conditions, the experimentally measured electrical AC voltage was first converted to a DC source voltage by calculating its root-mean-square (RMS) value (Berjano, 2006) and then applied to the end surface of the active forceps tips, as shown in Figure 4.3(a). During the 5 s coagulation time, the RMS voltage remained as a constant of 61 V. The end surface of the ground forceps tip was set as 0 V. Electrical continuity was applied to all the inner surfaces. All other outside surfaces were set as electrical insulating, assuming no electrical current can go through these surfaces. For the thermal boundary conditions of heat transfer in solids and non-isothermal flow, the heat source (q_g in Eqs. (4.3) and (4.4)) of total power generation from the electrical field was applied to all domains as the thermal input. The top surface of the spinal fluid and all the outer surfaces of both forceps tips and thermistors were subject to free convection ambient temperature and convective heat transfer coefficient set to 25 $W/m^2 \cdot K$. For other surfaces on the side and bottom, thermal insulation was applied, assuming that there was no heat exchange across these surfaces.

For the non-isothermal flow, which was only applied to the spinal fluid layer, the top surface of the spinal fluid is set as slip wall, assuming there were no viscous effects at the boundary and the bottom and side surfaces (the surface contacting with the spinal cord) were set to non-slip wall, which means the flow velocity on the wall is zero ($\mathbf{u}$=0).

The model was solved by COMSOL Multiphysics 4.2 (Burlington, MA) with direct PARDISO solver (Shenk and Gärtner, 2004). A personal computer with six cores (3.2 GHz) and 24 GB random-access memory (RAM) was used to perform the computational work. The computational time for the model with final mesh was about 48 hours.

4.3 Results

4.3.1 Validation of FEM with Experimental Measurements

Figure 4.4 shows the comparison of experimentally measured tissue temperature with the FEM predictions during the bipolar coagulation. The temperatures at the three measurement points, midpoint, 1.0, and 2.0 away from the forceps tips (Figure 4.3(a)) are presented. The overall average error is 4.2%. The maximum error for midpoint, 1.0, and 2.0 mm are 6.9%, 3.5%, and 12.6%, respectively.

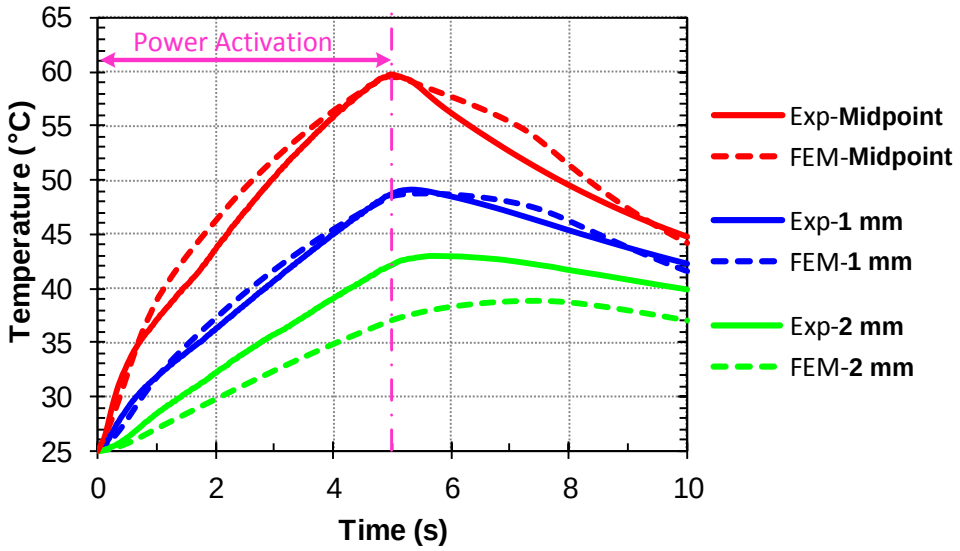

Figure 4.4 Comparison of the temperature profiles of experimental and FEM results at the three measurement points

4.3.2 Spatial and Temporal Temperature Distributions and Thermal Dose

Figure 4.5 shows the spatial and temporal temperature distribution of the cross-sectional plane. The maximum temperature occurs at the tissue and spinal fluid right next to the forceps tips, because there has the highest current density and strongest effect of Joule heating.

The lesion region can be defined as where tissue temperature is over 50°C (Tungjitkusolmun *et al.*, 2002) and is marked by the black line. The lesion region reaches the maximum width at 5 s. At this moment, the region has a 5 mm width and is 1.0 mm deep. At 6 s (1 s after power shut off), the region of tissue with temperature over 50°C

remains 4.8 mm wide and propagates deeper to 1.1 mm. At 10 s, all the tissue temperature falls below 50°C.

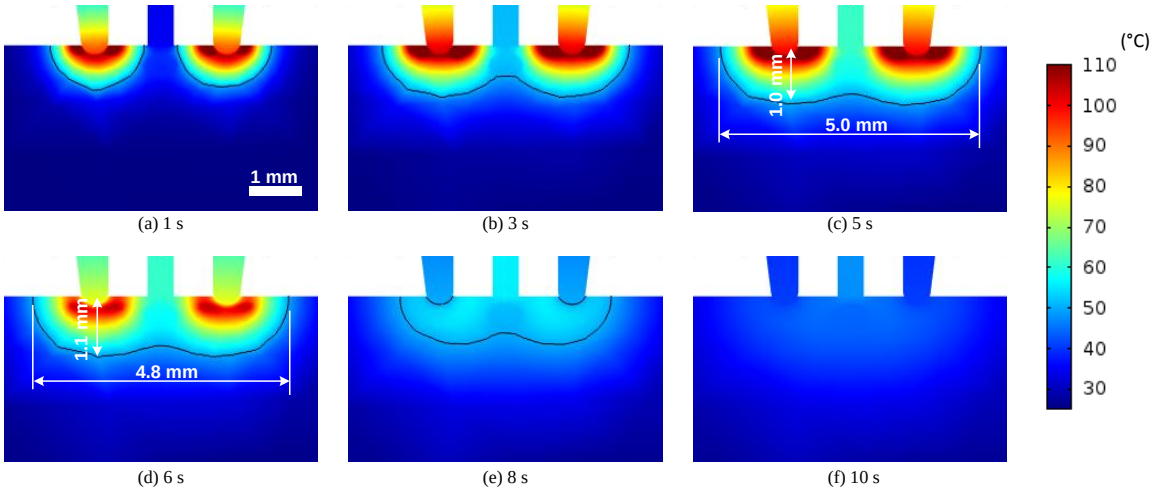

Figure 4.5 Cross-sectional view of temperature distribution. The black lines mark the boundary of 50°C

Figure 4.6 shows the simulated temperature profiles at the four points as marked as A, B, C, and D in Figure 4.3(b). Point A is at the tip of the bipolar forceps. Points B and C are 0.5 mm and 1.0 mm below Point A, respectively. Point D is at the center of the spinal artery. For point A, the temperature increases rapidly to 90°C in about only 0.5 s. The temperature rise then slows down because the latent heat is being accumulated. When the temperature exceeds 105°C, the electrical conductivity of spinal tissue decreases to 0.01 (S/m) due to the water loss (Chen *et al.*, 2012). This decrease on the electrical conductivity weakens the effect of Joule heating, so that the temperature rise remains slow throughout the rest of the power activation time. The temperature drops quickly immediately after the activation stops, but then slows down because the tissue is releasing the latent heat. Once all the latent heat is released (at 7 s), the temperature descending rate becomes proportional to the temperature gradient to the surrounding tissue.

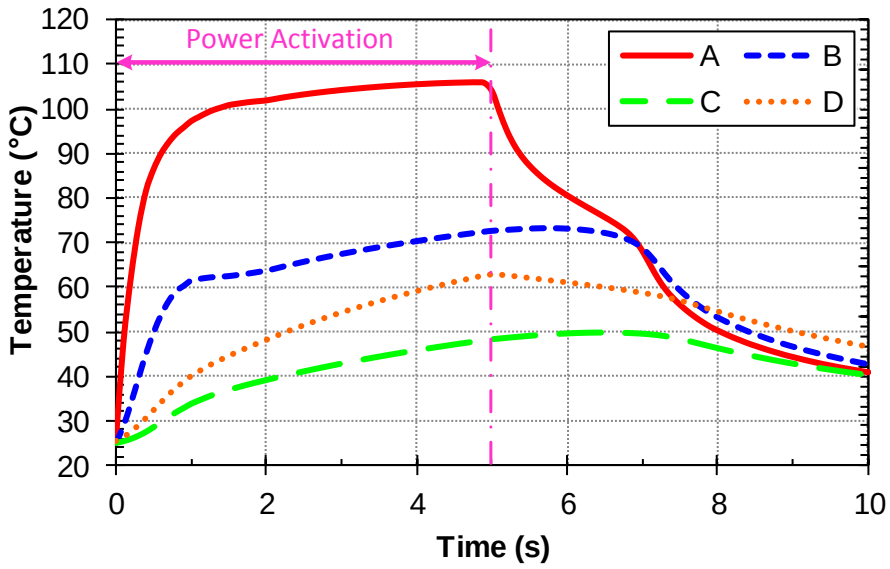

Figure 4.6 Simulated temperature profiles at points A: tip of the forceps, B: 0.5 mm below point A, C: 1.0 mm below point A, and D: center of the spinal artery

The temperature profiles at Points B and C follow the trend of Point A during the power activation time, but in a smaller scale. After the activation, the temperature continues increasing for about 1 s due to the heat conducted from Point A. The temperature of Point B decays slower than that of Point A because Point A contacts with the bipolar forceps (stainless steel) which has higher thermal conductivity than that of spinal cord and conducts heat away more efficiently. As a result, the temperature of Point B remains above 50°C for 8 s (from 0.5 – 8.5 s). The temperature at the center of the spinal artery (Point D) rises slowly and reaches 59°C at the end of power activation. Considering the coagulation temperature of 50°C (Sapareto and Dewey, 1984), the temperature at center of the artery increases to this level in 2.2 s.

Cumulative equivalent minutes at 43°C (CEM_{43}) is the most common thermal dose model to evaluate thermal damage in a variety of tissues (Dewhirst *et al.*, 2003). Thermal dose, CEM_{43} as a function of both temperature and time can be calculated as:

$$CEM_{43} = \sum_{t=0}^{t=final} \Delta t \cdot R^{(43-\bar{T})} \tag{4.11}$$

where Δt is the time interval, R is a constant equal to 0.25 when T<43°C and 0.5 when T>43°C, and $\bar{T}$ is the average temperature during the time interval Δt (Dewhirst *et al.*, 2003). The thermal dose for points A, B, C, and D were calculated. For points A, B, and C, the CEM_{43} values are higher than 1000 at the end of activation (t = 5 s) which are higher than the threshold value (>240) to cause gross appearance thermal damage (Yarmolenko *et al.*, 2011). For point C, the CEM_{43} is 0.71 when t = 5 s and reaches 9.33 when t = 10 s, which is in the range (0-20) of causing thermal damage that can be examined by histopathology (Yarmolenko *et al.*, 2011).

4.3.3 Effect of Non-Isothermal Flow

The effect of the non-isothermal flow can be seen by Figure 4.7. Compared to the model with both heat transfer in solids (denoted as Solid) and non-isothermal flow (denoted as Solid & Flow), the Solid model shows higher temperature at the midpoint. For the temperature at 1 mm, the Solid model shows close temperature as the Solid & Flow model during the first 5 s activation. After the activation stops, the temperature of Solid & Flow model decreases faster than the Solid model, as the heat can be carried away by the non-isothermal flow. For the temperature at 2 mm, the Solid model shows a slower temperature increase in the beginning but eventually reaches the same level as that of the Solid & Flow model because the Solid Model has a higher temperature at 2 mm after 6 s.

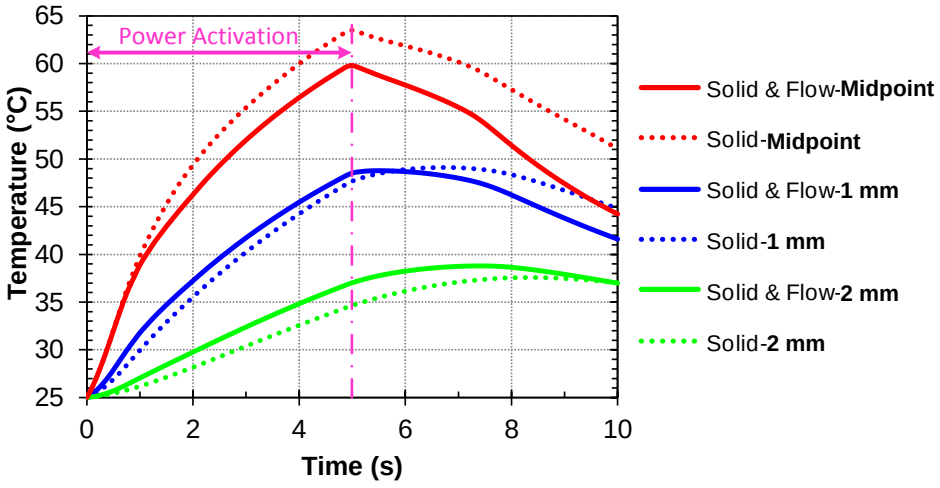

Figure 4.7 Comparison of temperature profiles between models with both heat transfer in solids and non-isothermal flow (Solid & Flow) and model with heat transfer in solids only (Solid).

4.4 Discussion and Conclusions

Three uncertain parameters in the FEM are: (i) thickness of the spinal fluid layer, (ii) wall thickness of the artery, and (iii) depth of the artery. For the thickness of the spinal fluid layer, it is estimated by calculating the electrical resistance value between the two forceps tips. Both the voltage and current consumption were recorded during the experiment that allows the calculation of the electrical resistance between the two tips. In the FEM, the thickness of the spinal fluid was adjusted to match the electrical resistance between the two tips. The electrical resistance value in the FEM was calculated by integrating the current density over the surfaces of forceps tips that contact with either the spinal fluid or the spinal cord to get the total current value. The electrical resistance can be obtained by dividing the input voltage over the total current.

A sensitivity analysis was performed to evaluate effect of the other two uncertain factors, the wall thickness and the depth of the artery. The wall thickness was varied from 0.01 to 0.1 mm (0.05 mm was used in this model) and resulting temperature profiles did not differ more than 1°C in all three thermistor positions. For the depth of the artery, a range between 0.26 to 0.5 mm was tested (0.3 mm was used in this model). Given the radius of the artery is 0.25 mm (0.5 mm diameter), the depths of 0.26 mm and 0.50 mm correspond to the distances between the top of the artery to the spinal cord surface of 0.01 and 0.25 mm, respectively. For depth that is smaller than 0.35 mm, the variation of temperature among different depths at all three points is less than 1°C. When the depth is increased to 0.5 mm, the temperature at 2.0 mm at the end of 5 s is 2.6°C lower than that of 0.3 mm depth. The reason is that the artery wall has a lower electrical conductivity than that of spinal cord tissue. When the artery is very close to the spinal cord surface, the artery wall forms a barrier for electrical current and thus forces the current to spread out further. Since the spinal artery is visible, a shallow depth is expected.

This study demonstrated that a thermo-electrical FEM with the combination of heat conduction in solids and non-isothermal flow could accurately predict the spatial and temporal temperature distribution during bipolar coagulation on spinal artery. As predicted in the model (Figure 4.5), the highest temperature occurs at the surrounding of the forceps tips. Therefore, it would be recommended that when performing coagulation, the forceps tips should be placed as close as possible to best use the generated heat and

minimize the thermal damaged region. The lesion region and size were identified with the FEM. While the coagulation is usually done with the existence of cerebrospinal fluid or irrigation, the effect of the fluid flow needs to be considered when modeling this procedure. This model can be further applied to study the thermal dose of tissue under coagulation and different waveforms to deliver electrical energy to minimize the lesion region.

References

Arakawa Y 2005 Application of the bipolar forceps with heat pipe technology (IsoCool) in neurosurgery *Japanese Journal of Neurosurgery* **14** 698-705

Arps J 1953 The effect of temperature on the density and electrical resistivity of sodium chloride solutions *Journal of Petroleum Technology* **5** 17-20

Berjano E J 2006 Theoretical modeling for radiofrequency ablation: state-of-the-art and challenges for the future *Biomed Eng Online* **5** 24

Brydon H, Hayward R, Harkness W and Bayston R 1995 Physical properties of cerebrospinal fluid of relevance to shunt function. 1: The effect of protein upon CSF viscosity *Br. J. Neurosurg.* **9** 639-44

Chehrazi B and Collins Jr W F 1981 A comparison of effects of bipolar and monopolar electrocoagulation in brain *J. Neurosurg.* **54** 197-203

Chen R, Chastagner M, Dodde R and Shih A 2012 Electrosurgical vessel sealing tissue temperature: experimental measurement and finite element modeling *Accepted by IEEE Trans on Biomed Eng*

Dewhirst M, Viglianti B, Lora-Michiels M, Hanson M and Hoopes P 2003 Basic principles of thermal dosimetry and thermal thresholds for tissue damage from hyperthermia *Int. J. Hyperthermia* **19** 267-94

Dodde R, Shih A and Advincula A P 2009 A novel technique for demonstrating the real-time subsurface tissue thermal profile of two energized surgical instruments *J. Minim. Invasive Gynecol.* **16** 599-603

Duck F A 1990 *Physical properties of tissue: a comprehensive reference* (London: Academic Press)

Edgerton R H 1975 Radial conductivity of arterial walls *Med. Biol. Eng. Comput.* **13** 531-4

Elliott-Lewis E W, Jolette J, Ramos J and Benzel E C 2010 Thermal damage assessment of novel bipolar forceps in a sheep model of spinal surgery *Neurosurgery* **67** 166-72

Elliott-Lewis E W, Mason A M and Barrow D L 2009 Evaluation of a new bipolar coagulation forceps in a thermal damage assessment *Neurosurgery* **65** 1182-7

Gabriel C, Gabriel S and Corthout E 1999 The dielectric properties of biological tissues: I. Literature survey *Phys. Med. Biol.* **41** 2231

Golombeck M A, Dossel O, Saubert A and Tonnier V M 1999 Magnetic resonance imaging with implanted neurostimulators: a first numerical approach using finite integration theory. In: *International Symposium on Electromagnetic Compatibility*, (Magdeburg, Germany

Gonzalez A, Ramos A, Green N, Castellanos A and Morgan H 2000 Fluid flow induced by nonuniform ac electric fields in electrolytes on microelectrodes. II. A linear double-layer analysis *Physical Review E* **61** 4019

Green N, Ramos A, Gonzalez A, Morgan H and Castellanos A 2000 Fluid flow induced by nonuniform ac electric fields in electrolytes on microelectrodes. I. Experimental measurements *Physical Review E* **61** 4011

Green N G, Ramos A, Gonzalez A, Castellanos A and Morgan H 2001 Electrothermally induced fluid flow on microelectrodes *J. Electrostatics* **53** 71-87

Greenwood Jr J 1940 Two point coagulation: a new principle and instrument for applying coagulation current in neurosurgery *Am. J. Surg.* **50** 267-70

Haemmerich D, Chachati L, Wright A S, Mahvi D M, Lee F T, Jr. and Webster J G 2003 Hepatic radiofrequency ablation with internally cooled probes: effect of coolant temperature on lesion size *IEEE Trans. Biomed. Eng.* **50** 493-500

Kraus A D, Welty J R and Aziz A S 2012 *Introduction to thermal and fluid engineering* (Boca Raton: CRC/Taylor & Francis)

Malis L I 1967 ed R M P Donaghy and M G Yasargil (Saint Louis: C. V. Mosby Co) pp 126-30

Martin G T and Angelone L 2009 Multiphysics model of the NovaSure endometrial ablation procedure. In: *The COMSOL Conference*, (Boston, MA

Mikami T, Takahashi A, Hashi K, Gasa S and Houkin K 2004 Performance of bipolar forceps during coagulation and its dependence on the tip material: a quantitative experimental assay. Technical note *J. Neurosurg.* **100** 133-8

Pennes H H 1948 Analysis of tissue and arterial blood temperatures in the resting human forearm *J. Appl. Physiol.* **1** 93-122

Ramos A, Morgan H, Green N and Castellanos A 1999a AC electrokinetics: a review of forces in microelectrode structures *Journal of Physics D: Applied Physics* **31** 2338

Ramos A, Morgan H, Green N G and Castellanos A 1999b AC electric-field-induced fluid flow in microelectrodes *J. Colloid Interface Sci.* **217** 420-2

Sapareto S A and Dewey W C 1984 Thermal dose determination in cancer therapy *Int. J. Radiat. Oncol. Biol. Phys.* **10** 787-800

Tungjitkusolmun S, Staelin S T, Haemmerich D, Tsai J Z, Cao H, Webster J G, Lee Jr F T, Mahvi D M and Vorperian V R 2002 Three-dimensional finite-element analyses for radio-frequency hepatic tumor ablation *IEEE Trans. Biomed. Eng.* **49** 3-9

Tungjitkusolmun S, Woo E J, Cao H, Tsai J Z, Vorperian V R and Webster J G 2000 Thermal-electrical finite element modelling for radio frequency cardiac ablation: effects of changes in myocardial properties *Med Biol Eng Comput* **38** 562-8

Yang D, Converse M C, Mahvi D M and Webster J G 2007 Expanding the bioheat equation to include tissue internal water evaporation during heating *IEEE Trans. Biomed. Eng.* **54** 1382-8

Yarmolenko P S, Moon E J, Landon C, Manzoor A, Hochman D W, Viglianti B L and Dewhirst M W 2011 Thresholds for thermal damage to normal tissues: An update *Int. J. Hyperthermia* **27** 320-43

CHAPTER 5
MULTI-MODALITY GELLAN GUM-BASED TISSUE-MIMICKING PHANTOM WITH TARGETED MECHANICAL, ELECTRICAL, AND THERMAL PROPERTIES

ABSTRACT

Presented in this study is a new class of gellan gum-based tissue-mimicking (TM) phantom material and a model to predict and control the elastic modulus, thermal conductivity, and electrical conductivity by adjusting the mass fractions of gellan gum, propylene glycol, and sodium chloride, respectively. Gellan gum is advantageous for its gelling efficiency to achieve outstanding mechanical properties (elastic modulus and toughness). A regression model for quantitative predictions of three material properties (elastic modulus, thermal conductivity, and electrical conductivity) was found based on the composition. A spinal cord gellan gum TM phantom formulated based on these regression models was made to closely match the mechanical, thermal, and electrical properties of porcine spinal cord. To validate the model and approach, this phantom was tested under bipolar electrosurgical coagulation and has been demonstrated that the phantom can produce similar temperature response as the spinal cord tissue.

Contents of this chapter will be submitted to *Physics in Medicine and Biology* as Roland K. Chen and Albert J. Shih, "Multi-Modality Gellan Gum-Based Tissue-Mimicking Phantom with Targeted Mechanical, Electrical, and Thermal Properties."

5.1 Introduction

Tissue-mimicking (TM) phantoms are widely used as a surrogate of tissue to study the performance of medical devices and treatment methods. Gellan gum, an extracellular anionic polysaccharide, was first discovered in 1978 (Giavasis *et al.*, 2000) as an alternate to gelatin and agar in food, pharmaceutical industries, gel electrophoresis, and cell culture (Bajaj *et al.*, 2007). The key advantages of gellan gum are the high gelling efficiency and ability to produce a wide spectrum of mechanical properties (Sworn, 2009). Gellan gum requires a third to a half the of gelatin and agar to achieve similar levels of mechanical strength (Morris *et al.*, 2012). Gellan gum also has good thermal stability (Lorenzo *et al.*, 2013) and flexibility of properties necessary to mimic soft tissues. Until recently the research of gellan gum has been limited to food industry (Evageliou *et al.*, 2010b). With this study we propose to use gellan gum as the gelling agent for TM phantom with specific mechanical, electrical, and thermal properties. This TM phantom can be used for electrosurgery and radiofrequency ablation.

Having equivalent properties to tissue is the most important requirement for a TM phantom. Material properties of TM phantom that have been manipulated in previous studies are summarized in Table 5.1. Modifiers to tailor different material properties are also listed in Table 5.1. TM phantoms are usually made of either chemically synthesized polymer (CSP) (e.g. silicone and polyvinyl chloride (PVC)) or biopolymer (e.g. gellan gum, gelatin, and agar). CSPs have a wider variety of mechanical properties and have good long-term stability over biopolymers because they do not contain water. CSPs are generally good electrical insulators; although addition polymerization with radicals or ions can make them electrically conductive (Guimard *et al.*, 2007). However, CSPs have much lower thermal conductivities and specific heats than those of soft tissue. Thus, CSPs are ideal for mechanically oriented TM phantom, but not for thermally or electrically related purposes. On the other hand, biopolymers, which usually consist of two basic components, gelling agent and water, is more tissue-like in many aspects as both biopolymer and soft tissue share high mass fraction of water (over 80%).

Table 5.1 Manipulated material properties in TM phantom

Category	Property	Modifier	Reference
Mechanical	Elastic modulus	Gelling agent	(Clark and Ross-Murphy, 1985)
	Strength	Salt, sugar	(Tang *et al.*, 1996; Evageliou *et al.*, 2010b)
	Fracture toughness	Gelling agent, salt, sugar	(Tang *et al.*, 1996; Evageliou *et al.*, 2010a)
Thermal	Conductivity	Oil, propylene glycol	(Craciunescu *et al.*, 1999; McDonald *et al.*, 2004)
	Specific heat	Aluminum powder	(Leonard *et al.*, 1984)
	Melting point	Formaldehyde	(Lazebnik *et al.*, 2005)
Electrical	Conductivity	Metal powder, sodium chloride, carbon	(Guy, 1971; Huang, 2002)
	Permittivity	Oil, Polyethylene	(Stuchly, 1980)
Acoustic	Scattering	Glass bead	(Madsen *et al.*, 1982)
	Impedance	*n*-propanol	(King *et al.*, 2007)
Optical	Absorption	Absorbing dye	(Iizuka *et al.*, 1999)
	Scattering	Albumen, serum	(Wagnieres *et al.*, 1999)
Relaxation	T1	Gadopentetic acid	(Mazzara *et al.*, 1996)
	T2	Agarose	(Ohno *et al.*, 2008)
Radiation	Attenuation	Resin	(White *et al.*, 1977)

Gellan gum is one such biopolymer. Biopolymers can be categorized into two types, proteinaceous and polysaccharide gels (Clark and Ross-Murphy, 1987). Gelatin is a proteinaceous gel material which is derived from natural collagen, such as porcine skin (Veis, 1964). Gelatin phantoms provide good elastic property but tend to have low melting temperatures, usually ranging from 27 to 30°C (Eldridge and Ferry, 1954). There are a wide variety of polysaccharide gelling agents, including agar, starch, and gellan gum (Clark and Ross-Murphy, 1987). Among these polysaccharide gels, agar is the most common one in applications such as bacterial culture support, food gelling, and many other uses in medicine and pharmacy. Agar provides stability over temperature up to 90°C and is thermo-reversible. However, agar phantoms are rather brittle and do not have tissue-like textures. Gellan gum is more elastic and can be tailored to different elastic moduli. The melting point of gellan gum can be up to 120°C. Therefore, gellan

gum was selected as the gelling agent in this study because it provides a basic platform to adjust to most of the soft tissue material properties and is compatible with most of the modifiers (see Table 5.1). In this study, we focus on the formulation of gellan gum TM phantom to achieve the targeted mechanical, electrical, and thermal properties. This gellan gum-based TM phantom gives a similar tactile feeling as soft tissues and can reproduce the thermal properties, making it ideal for a clinical simulator to train clinicians for electrosurgical procedures.

Mechanical properties have been studied for different types of phantom, including gelatin (Miller *et al.*, 1951; Bot *et al.*, 1996), agar (Clark *et al.*, 1983; Ross and Scanlon, 1999), and gellan gum (Lelievre *et al.*, 1992; Tang *et al.*, 1994). The elastic modulus – a measure of the structural stiffness of a phantom – generally increases with the concentration of the gelling agent (Clark and Ross-Murphy, 1985). Adding ions or sugar has been shown to increase elastic modulus and tensile/compression strengths (Tang *et al.*, 1996; Papageorgiou and Kasapis, 1995). Gelatin provides a variety of stiffnesses, depending on the concentration, and good fracture strength. Agar gel is usually stiffer but at the expense of being more brittle which does not reproduce soft tissue-like texture. However, gellan gum can be tailored made from stiff and brittle to soft and elastic, with an elastic modulus range from 0.3 to 200 kPa (Valli and Clark, 2010).

The electrical properties of TM phantom have been studied since the early 1980s (Stuchly, 1980). Since most of the mass fraction of TM phantom is water, ions can transport easily within the phantom and have comparable electrical conductivity to that of soft tissue. Sodium chloride (NaCl) is the most common agent to manipulate the electrical conductivity of biopolymer TM phantoms. Guy et al. (1971) first presented a phantom model for electrical conductivity. Solazzo et al. (2005) provided tabulated results of electrical conductivity versus the concentration of NaCl for agar phantom (in the range of about 0.1 to 10 wt%). Formulas for the fabrication of TM phantoms with accurate electrical conductivities exist for muscle (Chou *et al.*, 1985), liver (Stauffer *et al.*, 2003), hand (Gabriel, 2007), kidney (Lopresto *et al.*, 2011), and fat tissue (Yuan *et al.*, 2012). Lazebnik et al. developed an oil-in-gelatin phantom for a wideband use of microwave applications (Lazebnik *et al.*, 2005). Following the precedent of others, this

study selects NaCl as the modifier to control the electrical conductivity of the gellan gum material.

There are relatively few studies to investigate the thermal properties – the thermal conductivity and specific heat – of TM phantom. Leonard et al. perform the first study investigating the thermal conductivity and specific heat of TM phantom (Leonard *et al.*, 1984). Craciunescu et al. used an empirical equation provided by Perry and Green (Perry and Green, 1984) to formulate fat- and muscle-like tissue but showed a substantial difference between the measured and estimated thermal conductivity (Craciunescu *et al.*, 1999). Zhang et al. measured the thermal conductivity of agar at different concentrations and found that the thermal conductivity decreases as the concentration of agar increases (Zhang *et al.*, 2010). However, with the maximum concentration (10 wt%) of agar tested, which is close to the maximum solubility of agar in water, the thermal conductivity of agar phantom is still higher than most biological tissues (Duck, 1990), making it impossible to match tissue thermal conductivity by purely increasing the concentration of agar. The addition of propylene glycol (PPG) or oil has been shown to be able to reduce the thermal conductivity (Yuan *et al.*, 2012). PPG is selected as the modifier of thermal conductivity in the gellan gum based TM material in this study.

There is a paucity of study on TM phantom that considers both electrical and thermal properties. Yuan et al. modified the oil-in-gelatin phantom developed by Lazebnik et al. (2005) for tumor, muscle, and fat tissue with controlled thermal and electrical properties (Yuan *et al.*, 2012). With different combinations of water and vegetable oil, the thermal conductivity and specific heat is variable. The electrical properties agree with the soft tissue well while the thermal conductivity still shows a discrepancy up to 10%. The addition of oil to the phantom is based on the fact that tissue partially consists of oil. This is especially true of fat tissue. Oil has a lower specific heat (1.67 J/g·K) and thermal conductivity (0.17 W/m·K) than that of water (4.18 J/g·K and 0.60 W/m·K) so that adding oil can effectively decrease these two properties of a phantom.

This study develops a model to formulate gellan-gum based TM phantom materials to match the elastic modulus, electrical conductivity, and thermal conductivity of biological tissue for simulation of electrosurgery and radiofrequency ablation

procedures. A design of experiment method is used to evaluate the effects of gellan gum, PPG and NaCl concentration on three material properties (elastic modulus, electrical conductivity, and thermal conductivity). Regression model for each material property will then be developed. The procedure to formulate a desired TM phantom (in this case, spinal cord) based on regression models and experimental verification will be illustrated.

5.2 Material and methods

5.2.1 Components of the TM phantom

Table 5.2 lists five components that were used to make the TM phantom. Gellan gum is the gelling agent of the TM phantom. There are two forms of gellan gum, high-acyl and low-acyl forms. The high-acyl gellan gum provides soft and elastic texture while the low-acyl gellan gum gives firm and brittle texture (Valli and Clark, 2010). The high-acyl gellan gum was used in this study, as most of biological organs are soft tissues. Varying the concentration of high-acyl gellan gum can produce phantom tissues with different hardnesses but which remain elastic.

Table 5.2 Components of the TM phantom materials and their purposes

Component	Purpose
Gellan gum	Gelling agent, control of elastic modulus
Propylene glycol (PPG)	Control of thermal conductivity
NaCl	Control of electrical conductivity
Distilled water	Hydrate with gelling agent
Sodium propionate	Preservative, preventing grow of bacteria

The thermal conductivity of the gellan gum TM phantom is controlled by adding PPG. PPG has a lower thermal conductivity (0.17 W/m·K) than that of water (0.60 W/m·K). The thermal conductivity of most biological tissues ranges from 0.40 to 0.50 W/m·K (Duck, 1990). As water is the dominant mass fraction, adding PPG can effectively lower the thermal conductivity of the gellan gum-based TM phantom.

The electrical conductivity of the aqueous-based phantom can be adjusted by adding NaCl, as the disassociated ions can freely transport within water (Guy, 1971). Tabulated electrical conductivity vs. concentration of NaCl has been provided by Field and Hand (Field and Hand, 1990). However, the disassociation of NaCl will be affected with the

presence of PPG (Cheluget *et al.*, 1994). The more PPG is added in the solution, the less NaCl can be disassociated to conduct electrical current and the lower the electrical conductivity of the phantom will be. The relationship between the concentration of PPG and the electrical conductivity is expected to be nonlinear. This phenomenon has not been studied in the literature and was a key area of exploration in this study.

The rest of the compositions of the phantom are distilled water and sodium propionate. A very low concentration of sodium propionate (0.25 wt%) is added to inhibit the bacteria growth and help to preserve the phantom for long-term use. Such low concentrations were not expected to change the TM material properties.

5.2.2 Design of experiment

A single replicate 2^3 factorial design of experiment was first established (Montgomery, 2008). The three factors are the concentrations of gellan gum (A), PPG, (B), and NaCl (C). Each factor has two levels of concentration (high and low), as listed in Table 5.3. As shown in Table 5.4, this 2^3 design has eight possible combinations, marked as Phantoms #1 to #8. Phantom samples of all these eight combinations were made and the results were used to test the significance of each factor on each material property by ANOVA (p<0.05). An additional eight points at middle levels of three factors were then employed to investigate the nonlinear effect on three material properties. These samples are labeled as Phantoms #9 to #16. The aforementioned combinations can be visualized in Figure 5.1. For each phantom, the elastic modulus, thermal conductivity, and electrical conductivity were measured. To test the reproducibility of the phantom, a duplicate combination was made (Phantoms # 12 and 16). The experimental order, listed in Table 5.4, was randomly assigned to reduce any potential influence from the environment.

Table 5.3 Concentrations of each factor at the three different levels

	Level		
Factor	High (+)	Middle (o)	Low (−)
Gellan Gum	4%	2.5%	1%
PPG	40%	20%	0%
NaCl	0.2%	0.125%	0.05%

Table 5.4 Levels of TM phantom components and experimental order

Phantom #	Factor			Experimental order
	Gellan Gum	PPG	NaCl	
1	−	−	−	5
2	+	−	−	6
3	−	+	−	2
4	+	+	−	1
5	−	−	+	8
6	+	−	+	4
7	−	+	+	3
8	+	+	+	7
9	−	+	o	12
10	+	−	o	14
11	o	−	o	10
12	o	o	o	9
13	o	+	o	13
14	o	o	+	16
15	o	o	−	11
16	o	o	o	15

+: High level, −: low level, and o: central level

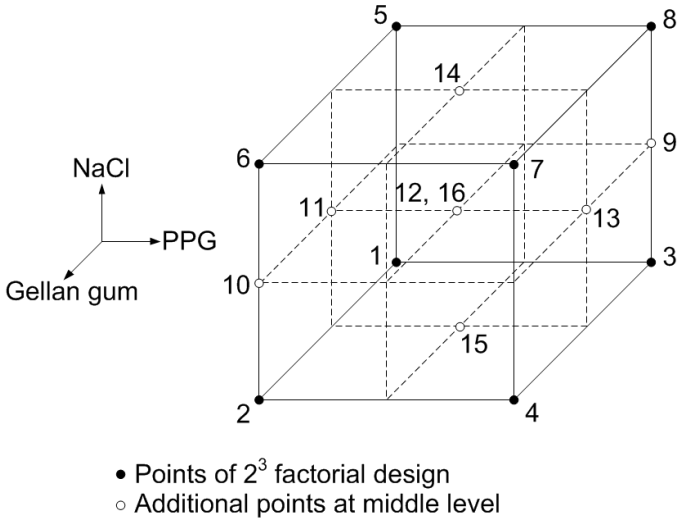

Figure 5.1 Visualization of the experimental design

5.2.3 Procedure of phantom manufacturing

Each phantom was made to have a total weight of 50 g. The weight of each component for a specific phantom can be calculated based on Table 5.3 and Table 5.4. Because the mass fraction is small, a premade 0.9% NaCl solution was used to add a precise amount of NaCl. The preservative, sodium propionate (Pronto Food Co., Chicago, IL, USA) had a fixed amount of 0.25 wt% for all phantom samples. The remaining mass fraction was filled by distilled water (Aqua solutions, Deer Park, TX, USA). The high-acyl gellan gum (Kelcogel® LT100, Modernist Pantry, York, ME, USA), sodium propionate, PPG (PTI Process Chemicals, Ringwood, IL, USA), distilled water, and 0.9% NaCl solution were added into a beaker sequentially. The solution was manually stirred until the gellan gum powder was dissolved. The solution was covered with aluminum foil and sat for 15 minutes before heating. A convective heating oven (Model 31197, Hamilton Beach, Richmond, VA, USA), set at 110°C, was used to heat the phantom solution for 40 minutes. During the heating process, the phantom solution was stirred every 10 minutes. The gelled phantom was cooled down at room temperature for three hours before any further testing.

5.2.4 Measurement of material properties and electrosurgery experiment

- *Elastic modulus*

As shown in Figure 5.2(a), the elastic modulus was measured by indentation test with a Type 000-S durometer (Instron, Norwood, MA, USA), which is designed to measure the hardness of soft material using a sphere surface indenter. The sphere radius of this indenter (Figure 5.2(d)) has a radius of 10.67 mm. The durometer was attached to a linear stage (Model 200cri, Siskiyou instruments, Grants Pass, OR, USA) to control the contact between the indenter and the phantom under testing. The durometer reading was converted to elastic modulus (E) based on the equation (Briscoe *et al.*, 1999):

$$E = \frac{(1-\upsilon^2)\cdot F}{4\sqrt{R}\cdot h^{3/2}} \tag{5.1}$$

where υ is Poisson's ratio, F is the spring force of the durometer, R is the radius of the sphere indenter, and h is the indentation depth. The Poisson's ratio was assumed to have

a constant value, 0.32 for all the phantoms (Ross and Scanlon, 1999). The F (unit: N) and h (unit: m) can be obtained from the durometer dial reading (H) as relationship between the spring force and indentation depth is given by the American Society for Testing and Materials (ASTM Standard D2240 - 05) as follow.

$$F = 0.01765 \cdot H + 0.167 \tag{5.2}$$

and

$$h = 0.005(1 - \frac{H}{100}) \tag{5.3}$$

where 0.005 is the extension length of the indenter and 100 is the maximum dial reading. Each phantom was measured by the durometer for three times and the averaged value was used.

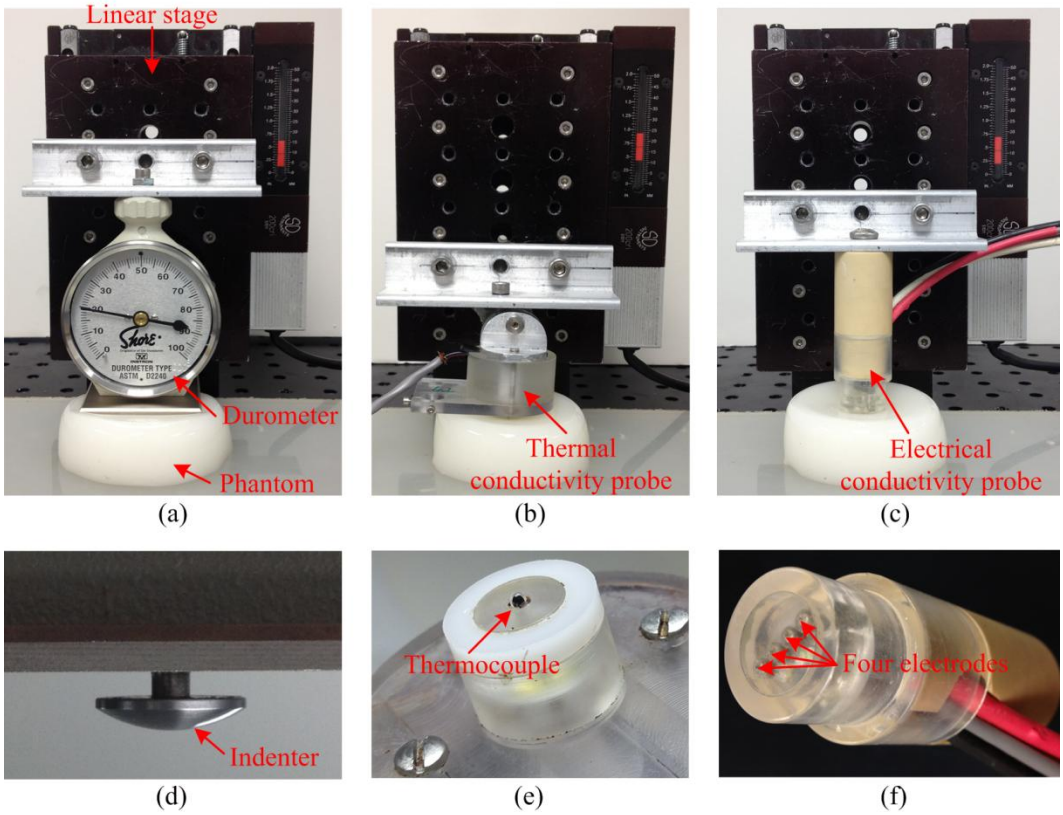

Figure 5.2 Experimental setup for measuring (a) elastic modulus, (b) thermal conductivity, and (c) electrical conductivity and close up views of (d) indenter of durometer, (e) thermal conductivity probe, and (f) electrical conductivity probe

- *Thermal conductivity*

Figure 5.2(b) shows the experimental setup for measuring thermal conductivity with a self-heated thermistor method first developed by Chato (Chato, 1968) and further advanced by Valvano (Valvano *et al.*, 1985). A single thermistor (P60DA102M, GE, Fairfield, CT, USA) with a diameter of 1.52 mm, as shown in Figure 5.2(e), was inserted into the phantom. The thermistor was used to deliver heat and monitor the temperature at the same time. Constant current (0.1 mA) was applied to the thermistor for the first 5 s to determine the initial temperature of the phantom. After resting for 10 s, a constant 5 V was applied to the thermistor, which was in series with a preset resistor (932 ohm), for 30 s. Measuring the voltage difference across the preset resistor determined the total current. The temperature change during the 30 s heating time was recorded by the thermistor. This temperature change over time was then fitted into an empirical equation to determine the thermal conductivity of the phantom. Details about how to calculate the thermal conductivity based on the temperature change with an empirical equation are described in Patel *et al.*, 1987.

- *Electrical conductivity*

The electrical conductivity was measured using a standard tetrapolar technique (Ackmann, 1993; Gabriel *et al.*, 1996), as shown in Figure 5.2(c). A custom circuit and measurement probe described in (Dodde *et al.*, 2012) was used to perform the measurement of electrical conductivity at 13 frequencies ranging from 100 to 1M Hz (100, 200 500, 1000, etc.). The electrical conductivity probe has four 0.25 mm diameter platinum electrodes with 3 mm spacing, as shown in Figure 5.2(f). A 60 μA root-mean-square current was generated by the circuit to ensure the effect of resistive heating is negligible. The current was sent to the first electrode and return from the fourth electrode. The voltage difference between the second and the third electrodes was recorded, allowing for the calculation of electrical conductivity. The resistance value between the second and the third electrode was calculated by dividing the voltage difference with the input current. As the geometric constant of the probe (53.05 (1/m)) is known (Dodde *et al.*, 2012), the electrical conductivity of phantom can be determined by dividing the geometric constant with the measured resistance value (Littwitz *et al.*, 1990).

- *Electrosurgery experiment*

To validate the ability of the TM phantom with targeted material properties to reproduce the temperature response to electrosurgical device, bipolar forceps (DePuy Codman & Shurtleff, Warsaw, IN, USA) were used to perform coagulation on the TM phantom, as shown in Figure 5.3(a). The temperature was measured at three points, midpoint between the forceps tips, 1 and 2 mm away from the midpoint along the centerline, as illustrated in Figure 5.3(b). The resulting temperature profiles were compared to the experimental results done in a porcine spinal cord presented in another study by the authors (Chen *et al.*, Submitted). The TM phantom used in this experiment has the targeted material properties close to those of soft tissue, which will be illustrated in Section 3.3. The bipolar forceps were powered by an electrosurgical generator, Valleylab Force FX (Covidien, Boulder, CO, USA) with 25 Malis units. The coagulation time was fixed at 5 seconds. Five coagulations were performed on the same TM phantom at different locations.

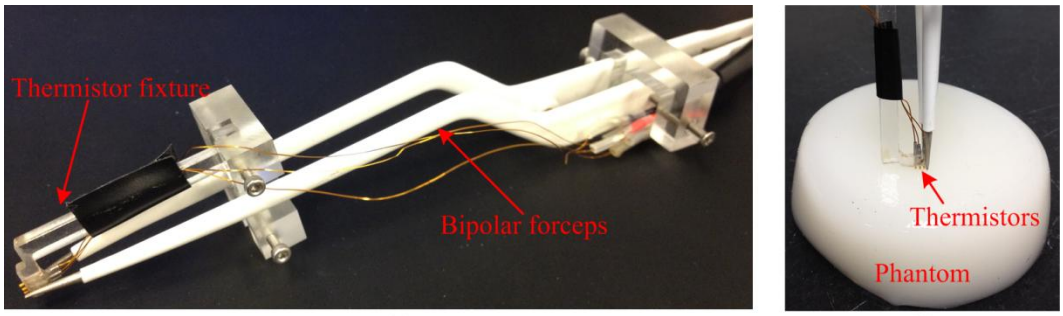

Figure 5.3 (a) Bipolar forceps with temperature measurement setup used to coagulate TM phantom and (b) coagulating on TM phantom

5.3 Results

5.3.1 Measured TM phantom material properties

The hardness, thermal conductivity, and electrical conductivity for all 16 phantoms were measured and are summarized in Table 5.5. The hardness of the tested phantoms ranges from 21 to 49, which corresponds to elastic moduli from 9.12 to 23.30 kPa. For thermal conductivity, the value varies from 0.400 to 0.574 W/m·K. The electrical conductivity has a wide range, from 0.091 to 0.612 S/m. The electrical

conductivity remains relatively constant over the measuring frequency range (100 Hz to 1 MHz). The results shown in Table 5.5 are the electrical conductivity at 500 kHz, which is close to the frequency used in electrosurgery. The differences between the two replicate phantoms (Phantom # 12 and 16) for elastic modulus, thermal conductivity, and electrical conductivity are 1.8%, 0.6%, and 2.8%, respectively. This very small discrepancy highlights the reproducibility of the phantom and repeatability of the experiment.

Table 5.5 Measurement results of phantom material properties

Phantom #	Elastic Modulus (kPa)	Thermal conductivity (W/m·K)	Electrical conductivity at 500k Hz (S/m)
1	9.12	0.574	0.322
2	18.10	0.537	0.396
3	12.06	0.427	0.091
4	18.76	0.404	0.132
5	8.02	0.560	0.588
6	19.45	0.532	0.612
7	10.31	0.424	0.210
8	23.30	0.400	0.206
9	9.51	0.405	0.181
10	17.46	0.526	0.526
11	11.60	0.556	0.479
12	15.09	0.495	0.313
13	16.23	0.400	0.195
14	14.54	0.491	0.385
15	13.01	0.485	0.239
16	14.82	0.498	0.322

The ANOVA results of the significance of each factor on the three material properties are listed in Table 5.6. The concentrations of both gellan gum and PPG had a significant effect on the elastic modulus of phantom. Although it has been shown that the concentration of ions will affect the elastic modulus of phantom, the non-significant result for NaCl may be contributed to the small varying range of the NaCl concentration. For thermal conductivity, only the concentration of NaCl does not have a significant effect. For electrical conductivity, the main effects of PPG and NaCl and the interaction

between PPG and NaCl are significant. The concentration of PPG has significant effect on all three material properties. Extra care must be taken when formulating phantom with PPG, regardless which material property is of interested.

Table 5.6 ANONA results of the effect of factors on the three material properties

	p value		
Factor	Elastic Modulus	Thermal conductivity	Electrical conductivity
Gellan Gum	0.014*	0.0018*	0.73
PPG	<0.001*	<0.001*	<0.001*
NaCl	0.15	0.22	<0.001*
Interaction	-	-	0.01*

*Statistically significant

5.3.2 Regression models

The factors that were shown to be significant were included in the regression model. The regression model for each of the three material properties were developed with the method of least squares which included all the 16 phantoms. The coefficient of determination (R^2) was calculated to evaluate the predicting ability of the regression for each material property.

For elastic modulus, the relationship between elastic modulus and durometer dial reading is derived by substituting F and h in Eq. (5.1) by Eqs. (5.2) and (5.3), respectively and can be expressed as:

$$E = \frac{707.1 \cdot (1-\upsilon^2) \cdot (0.01765H + 0.167)}{\sqrt{R} \cdot (100-H)^{3/2}} \tag{5.4}$$

From Eq. (5.4), the durometer reading, H, which corresponds to the desired elastic modulus, can be found. The regression model for the targeting H is:

$$H = 16.46 + 651.458\, m_A + 13.29\, m_B \tag{5.5}$$

where m_A, m_B, and m_C are mass fraction of gellan gum, PPG, and 0.9% NaCl solution, respectively.

The regression model for thermal conductivity (k) is:

$$k = 0.576 - 0.986\, m_A - 0.36\, m_B \tag{5.6}$$

and the regression model for electrical conductivity (σ) is:

$$\sigma = 0.260 - 0.399\, m_B + 1.355\, m_C - 2.166\, m_B\, m_C, \tag{5.7}$$

The R^2 for elastic modulus, thermal conductivity, and electrical conductivity are 0.92, 0.97 and 0.95, respectively. These high R^2 values indicate that the regression model can explain more than 90% of the variance in each of the three material properties and can accurately predict the material property with different phantom compositions.

5.3.3 Formulation of targeted tissue properties

Given desired tissue properties, a phantom formula can be calculated based on the regression models. This research uses spinal cord as an example. Table 5.7 lists the key material properties of the spinal cord tissue. To match the 11.68 kPa elastic modulus of the spinal cord, from Eq. (5.4), the corresponding reading in 000-S hardness reading should be 30.2. The mass fractions of gellan gum (m_a) and PPG (m_b) can be solved simultaneously using Eqs. (5.5) and (5.6), given H and k equal to 24.4 and 0.503, respectively. Once m_a and m_b are found, the only one unknown, the mass fraction of 0.9% NaCl solution (m_c), can be solved by Eq. (5.7). The m_a, m_b, and m_c for spinal cord TM phantom are 1.8%, 15.4%, and 10.9%, respectively.

A gellan gum TM phantom based on this formula was made and the material properties (elastic modulus, thermal conductivity, electrical conductivity, density, and specific heat) were measured. The thermal diffusivity was calculated based on the thermal conductivity, density, and specific heat. The error percentage for each material property is summarized in Table 5.7. The errors of all these measured properties are all <3%. The density and specific heat are not controlled in the formula but only have 0.4% and 1.6% error, respectively. The components with major mass fractions (distilled water, PPG, and 0.9% NaCl solution) all have density that is close to the spinal cord tissue, so it

is expected that the resulting density of the spinal cord phantom will also be close. For specific heat, because the phantom and tissue both have a high mass fraction of water, which has high specific heat (4.18 kJ/kg·K), the specific heat was expected to be in a similar range.

Table 5.7 Comparison of material properties between the formulated spinal cord phantom and real tissue

Properties	Comparison		
	Real tissue	Phantom	Error
Elastic modulus (kPa)	11.68 [a]	12.02	2.9%
Thermal conductivity (W/m·K)	0.503 [b]	0.505	1.0%
Electrical conductivity [c] (S/m)	0.31 [c]	0.316	1.9%
Density (kg/m^3)	1035 [d]	1031	0.4%
Specific heat (kJ/kg·K)	3.72 [d]	3.66	1.6%
Thermal diffusivity (m^2/s)	1.31	1.34	2.3%

[a](Van Dommelen *et al.*, 2010), [b](Bowman *et al.*, 1975), [c](Gabriel *et al.*, 1996), and [d](Duck, 1990)

5.3.4 Validation of temperature response by TM phantom with targeted tissue properties

Experimental validation, as described in Section 5.2.4, was performed to examine the spinal cord phantom's ability to reproduce the temperature response found in porcine spinal cord tissue. The spinal cord TM phantom formulated in Section 5.3.3 was used for this validation. Figure 5.4 shows the temperature results of coagulation on both porcine spinal cord tissue as in the experiment conducted by the authors (Chen *et al.*, Submitted) and the spinal cord TM phantom. The error bars indicate the maximum and minimum temperature results among the five coagulation tests on the spinal cord phantom. The averaged temperature profiles of TM phantom at all the three measuring points match well with those of porcine spinal cord tissue and demonstrated the capability of the gellan gum-based TM phantom for electrosurgery simulator.

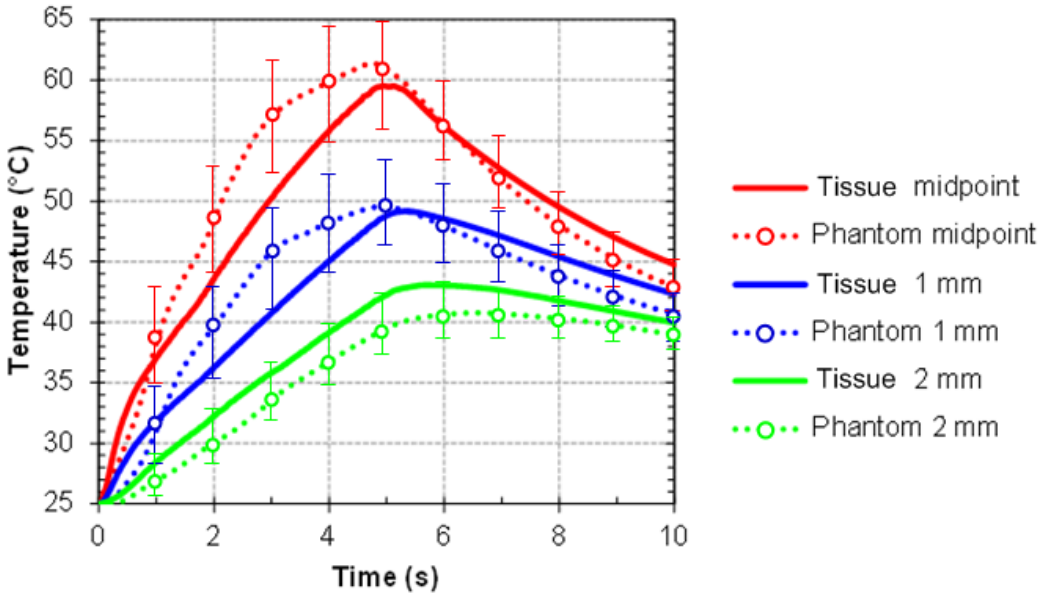

Figure 5.4 Temperature profiles of coagulation on porcine spinal cord (Tissue) and TM phantom (Phantom)

5.4 Conclusions

This study presented a systematic, model-based approach to find the composition of gellan gum-based TM phantom to achieve the desired elastic modulus, thermal conductivity, and electrical conductivity of soft tissue. The use of high-acyl gellan gum as a gelling agent successfully reproduced the tissue-like mechanical properties. The prediction models were verified by making a spinal cord TM phantom based on the gellan gum formula predicted by the model. This spinal cord TM phantom not only has close material properties (elastic modulus, thermal conductivity, electrical conductivity, density, specific heat, and thermal diffusivity) as the targeted tissue but also yielded a similar temperature response as the real spinal cord tissue in a bipolar electrosurgery experiment. These predictive models can be also used to formulate TM phantoms for other soft tissues.

A few limitations exist in this study. First, the electrical conductivity was measured only up to 1 MHz, which does not reach the level of radiofrequency. With the extensive work that has been done on the wideband measurement of electrical conductivity, it is expected that the electrical conductivity at radiofrequency range can be correlated to that found at 1 MHz (Dadd *et al*., 1996). Second, the range of elastic

modulus covered by the experiment data is approximately 9-23 kPa, which may be further expanded to include stiffer soft tissue, such as muscle. Third, the fracture toughness of the TM phantom was not measured or quantified. However, it has been shown that the fracture toughness of high-acyl gellan gum phantom can be over 70% strain rate (Valli and Clark, 2010) which is much higher than that of agar phantom (generally lower than 40%) (McEvoy *et al.*, 1985). With addition of cations, the toughness of gellan gum phantom can be increased to 110% strain rate (Tang *et al.*, 1996).

This study demonstrated the feasibility of using gellan gum for a new class of TM phantoms, providing a basic platform for further material property, such as acoustic scattering and radiation attenuation. It is possible to formulate a TM phantom with gellan gum for ultrasonic devices, fluoroscopy, or hyperthermia therapies. Gellan gum has the potential to replace agar and gelatin in making TM phantom for various clinical simulator applications.

References

Ackmann J J 1993 Complex bioelectric impedance measurement system for the frequency range from 5 Hz to 1 MHz *Annals of biomedical engineering* **21** 135-46

ASTM Standard D2240-05 2010 Standard Test Method for Rubber Property—Durometer Hardness (West Conshohocken: ASTM International) DOI: 10.1520/D2240-05R10

Bajaj I B, Survase S A, Saudagar P S and Singhal R S 2007 Gellan gum: fermentative production, downstream processing and applications *Food Technology and Biotechnology* **45** 341-54

Bot A, van Amerongen I A, Groot R D, Hoekstra N L and Agterof W G M 1996 Large deformation rheology of gelatin gels *Polymer Gels and Networks* **4** 189-227

Bowman H F, Cravalho E G and Woods M 1975 Theory, measurement, and application of thermal properties of biomaterials *Annual Review of Biophysics and Bioengineering* **4** 43-80

Briscoe B, Sebastian K and Adams M 1999 The effect of indenter geometry on the elastic response to indentation *Journal of Physics D: Applied Physics* **27** 1156

Chato J 1968 *A method for the measurement of the thermal properties of biological materials* (New York: American Society of Mechanical Engineers)

Cheluget E L, Gelinas S, Vera J H and Weber M E 1994 Liquid-liquid equilibrium of aqueous mixtures of poly (propylene glycol) with sodium chloride *Journal of Chemical and Engineering Data* **39** 127-30

Chen R, Than K, Park P and Shih A Submitted Comparison of thermal coagulation profiles for bipolar forceps with different cooling mechanisms in a porcine model of spinal surgery *Neurosurgery*

Chou C K, Chen G W, Guy A W and Luk K H 1985 Formulas for preparing phantom muscle tissue at various radiofrequencies *Bioelectromagnetics* **5** 435-41

Clark A, Richardson R, Ross-Murphy S and Stubbs J 1983 Structural and mechanical properties of agar/gelatin co-gels. small-deformation studies *Macromolecules* **16** 1367-74

Clark A and Ross-Murphy S B 1987 *Biopolymers,* ed K Dusek (London: Springer) pp 57-192

Clark A H and Ross-Murphy S B 1985 The concentration dependence of biopolymer gel modulus *British Polymer Journal* **17** 164-8

Craciunescu O I, Howle L E and Clegg S T 1999 Experimental evaluation of the thermal properties of two tissue equivalent phantom materials *International Journal of Hyperthermia* **15** 509-18

Dadd J, Ryan T and Platt R 1996 Tissue impedance as a function of temperature and time *Biomedical Sciences Instrumentation* **32** 205-14

Dodde R, Bull J and Shih A 2012 Bioimpedance of soft tissue under compression *Physiological measurement* **33** 1095-109

Duck F A 1990 *Physical properties of tissue: a comprehensive reference book* (London: Academic)

Eldridge J E and Ferry J D 1954 Studies of the cross-linking process in gelatin gels. III. Dependence of melting point on concentration and molecular weight *The Journal of Physical Chemistry* **58** 992-5

Evageliou V, Karantoni M, Mandala I and Komaitis M 2010a Compression of gellan gels. part I: effect of salts *International Journal of Food Science & Technology* **45** 1076-80

Evageliou V, Mazioti M, Mandala I and Komaitis M 2010b Compression of gellan gels. Part II: effect of sugars *Food Hydrocolloids* **24** 392-7

Field S B and Hand J W 1990 *An introduction to the practical aspects of clinical hyperthermia* (London ; New York: Taylor & Francis)

Gabriel C 2007 Tissue equivalent material for hand phantoms *Physics in Medicine and Biology* **52** 4205-10

Gabriel C, Gabriel S and Corthout E 1996 The dielectric properties of biological tissues: I. Literature survey *Physics in Medicine and Biology* **41** 2231-49

Giavasis I, Harvey L M and McNeil B 2000 Gellan gum *Critical Reviews in Biotechnology* **20** 177-211

Guimard N K, Gomez N and Schmidt C E 2007 Conducting polymers in biomedical engineering *Progress in Polymer Science* **32** 876-921

Guy A W 1971 Analyses of electromagnetic fields induced in biological tissues by thermographic studies on equivalent phantom models *IEEE Transactions on Microwave Theory and Techniques* **MTT-19** 205-14

Huang J C 2002 Carbon black filled conducting polymers and polymer blends *Advances in Polymer Technology* **21** 299-313

Iizuka M N, Sherar M D and Vitkin I A 1999 Optical phantom materials for near infrared laser photocoagulation studies *Lasers in Surgery and Medicine* **25** 159-69

King R L, Herman B A, Maruvada S, Wear K A and Harris G R 2007 Development of a HIFU phantom. In: *6th International Symposium on Therapeutic Ultrasound,* pp 351-6

Lazebnik M, Madsen E L, Frank G R and Hagness S C 2005 Tissue-mimicking phantom materials for narrowband and ultrawideband microwave applications *Physics in Medicine and Biology* **50** 4245-58

Lelievre J, Mirza I and Tung M 1992 Failure testing of gellan gels *Journal of food engineering* **16** 25-37

Leonard J B, Foster K R and Athley T 1984 Thermal properties of tissue equivalent phantom materials *IEEE Transactions on Biomedical Engineering* 533-6

Littwitz C, Ragheb T and Geddes L 1990 Cell constant of the tetrapolar conductivity cell *Medical and Biological Engineering and Computing* **28** 587-90

Lopresto V, Pinto R, Lodato R, Lovisolo G and Cavagnaro M 2011 Design and realisation of tissue-equivalent dielectric simulators for dosimetric studies on microwave antennas for interstitial ablation *Physica Medica* **28** 245-53

Lorenzo L, Zaritzky N and Califano A 2013 Rheological analysis of emulsion-filled gels based on high acyl gellan gum *Food Hydrocolloids* **30** 672-80

Madsen E L, Zagzebski J A and Frank G R 1982 Oil-in-gelatin dispersions for use as ultrasonically tissue-mimicking materials *Ultrasound in medicine & biology* **8** 277-87

Mazzara G, Briggs R W, Wu Z and Steinbach B G 1996 Use of a modified polysaccharide gel in developing a realistic breast phantom for MRI *Magnetic Resonance Imaging* **14** 639-48

McDonald M, Lochhead S, Chopra R and Bronskill M J 2004 Multi-modality tissue-mimicking phantom for thermal therapy *Physics in Medicine and Biology* **49** 2767

McEvoy H, Ross-Murphy S and Clark A 1985 Large deformation and ultimate properties of biopolymer gels: 1. Single biopolymer component systems *Polymer* **26** 1483-92

Miller M, Ferry J D, Schremp F W and Eldridge J E 1951 Studies of the cross-linking process in gelatin gels. II. static rigidity and stress relaxation *The Journal of Physical Chemistry* **55** 1387-400

Montgomery D C 2008 *Design and analysis of experiments* (New York: John Wiley & Sons)

Morris E R, Nishinari K and Rinaudo M 2012 Gelation of gellan-a review *Food Hydrocolloids* **28** 373-411

Ohno S, Kato H, Harimoto T, Ikemoto Y, Yoshitomi K, Kadohisa S, Kuroda M and Kanazawa S 2008 Production of a human-tissue-equivalent MRI phantom: optimization of material heating *Magnetic Resonance in Medical Sciences* **7** 131-40

Papageorgiou M and Kasapis S 1995 The effect of added sucrose and corn syrup on the physical properties of gellan-gelatin mixed gels *Food Hydrocolloids* **9** 211-20

Patel P, Valvano J, Pearce J, Prahl S and Denham C 1987 A self-heated thermistor technique to measure effective thermal properties from the tissue surface *Journal of Biomechanical Engineering* **109** 330-5

Perry R H and Green D W 1984 *Perry's chemical engineers' handbook* (New York: McGraw-Hill)

Ross K and Scanlon M 1999 Analysis of the elastic modulus of agar gel by indentation *Journal of Texture Studies* **30** 17-27

Stauffer P, Rossetto F, Prakash M, Neuman D and Lee T 2003 Phantom and animal tissues for modelling the electrical properties of human liver *International Journal of Hyperthermia* **19** 89-101

Stuchly M 1980 Dielectric properties of biological substances- tabulated *Journal of Microwave Power* **15** 19-26

Sworn G 2009 *Handbook of hydrocolloids*, ed G O Phillips and P A Williams (Cambridge, UK: Woodhead Publishing)

Tang J, Lelievre J, Tung M A and Zeng Y 1994 Polymer and ion concentration effects on gellan gel strength and strain *Journal of Food Science* **59** 216-20

Tang J, Tung M A and Zeng Y 1996 Compression strength and deformation of gellan gels formed with mono-and divalent cations *Carbohydrate polymers* **29** 11-6

Valli R and Clark R 2010 *Food Stabilisers, Thickeners and Gelling Agents*, ed A Imeson (New York: John Wiley & Sons)

Valvano J, Cochran J and Diller K 1985 Thermal conductivity and diffusivity of biomaterials measured with self-heated thermistors *International Journal of Thermophysics* **6** 301-11

Van Dommelen J, Van der Sande T, Hrapko M and Peters G 2010 Mechanical properties of brain tissue by indentation: Interregional variation *Journal of the Mechanical Behavior of Biomedical Materials* **3** 158-66

Veis A 1964 *The macromolecular chemistry of gelatin* (New York: Academic Press)

Wagnieres G, Cheng S, Zellweger M, Utke N, Braichotte D, Ballini J P and van den Bergh H 1999 An optical phantom with tissue-like properties in the visible for use in PDT and fluorescence spectroscopy *Physics in Medicine and Biology* **42** 1415-26

White D, Martin R and Darlison R 1977 Epoxy resin based tissue substitutes *British Journal of Radiology* **50** 814-21

Yuan Y, Wyatt C, Maccarini P, Stauffer P, Craciunescu O, MacFall J, Dewhirst M and Das S K 2012 A heterogeneous human tissue mimicking phantom for RF heating and MRI thermal monitoring verification *Physics in Medicine and Biology* **57** 2021-37

Zhang M, Che Z, Chen J, Zhao H, Yang L, Zhong Z and Lu J 2010 Experimental determination of thermal conductivity of water-agar gel at different concentrations and temperatures *Journal of Chemical & Engineering Data* **56** 859-64

CHAPTER 6
CONCLUSIONS AND FUTURE WORK

6.1 Conclusions

This dissertation studied the thermal spread during electrosurgical coagulation and developed a tissue-mimicking phantom for electrosurgery. Both experimental and modeling work was conducted to quantify the thermal spread. The results from this study enhance the understanding of both temperature distribution and thermal damage caused by coagulation. The developed tissue-mimicking phantom can be used to study the performance of electrosurgical devices and also as a training tool for surgeons.

The major achievements of this dissertation are:

- *A multi-physics two-phase model for bipolar coagulation on spinal cord with cerebrospinal fluid:*

  A comprehensive numerical analysis model with multi-physics, thermal and electrical fields, and two phases, liquid and solid, was developed to predict tissue temperature during bipolar coagulation. When coagulation was performed with the existence of cerebrospinal fluid, this fluid layer not only changed the electrical current dissipation but also affected the temperature distribution. These two fields and two phases were coupled in the COMSOL finite element model to allow for the accurate prediction of temperature. Modeling techniques were also developed to account for the water evaporation, change of material properties due to water loss, and tissue fusion. With this model, spatial and temporal temperature distributions can be obtained. Thermal dose of the spinal cord tissue at any given point can also be calculated to understand the level of thermal damage caused by coagulation.

- *A methodology to formulate gellan-gum based tissue-mimicking phantom with targeted material properties based on the design of experiment method:*

  A systematic approach was developed to formulate gellan-gum based tissue-mimicking phantom material with targeted mechanical, thermal, and electrical properties. Using the design of experiment method, the significant factors on each targeting material properties were identified. A regression model was then developed and used to calculate the formula for phantom of any desired soft tissue. This approach has been validated by making a spinal cord tissue-mimicking phantom. This phantom has close material properties to spinal cord tissue and can reproduce the temperature response to bipolar coagulation as the spinal cord tissue.

The original contributions of this dissertation are as follows:

(1) An experimental setup to measure the temperature profiles during bipolar coagulation.

(2) A comparison of temperature profiles induced by four different bipolar forceps, including regular stainless steel, titanium, active heat transfer, and SILVERGlide forceps. The heating effect and cooling effect of all these four forceps were analyzed. Different cooling techniques have different working range and reaction time.

(3) A finite element model accounting for evaporation, effect of water loss, and tissue fusion by manipulating material properties to predict tissue temperature during electrosurgical vessel sealing.

(4) A two-phase (solid and liquid) thermo-electrical model for bipolar coagulation with the existence of cerebrospinal fluid.

(5) Use of gellan-gum modified by glycol and NaCl as tissue-mimicking phantom material

(6) A regression model to formulate tissue-mimicking phantom with specific elastic modulus, thermal conductivity, and electrical conductivity.

6.2 Future Work

The experimental and modeling results of electrosurgical coagulation and the tissue-mimicking phantom can be further improved and expanded through the following directions:

(1) Investigation of thermal spread when performing electrosurgical coagulation in a moving situation. During the neurosurgery, the coagulation is often performed with the forceps tips dragging along a vessel. In this situation, the thermal spread may be different from that of the fixed situation.

(2) Development of an external cooling mechanism that can be incorporated with the current bipolar forceps to minimize the thermal spread. The existing bipolar forceps with cooling technique can only be used to control little amount of bleeding. In the case of heavy bleeding, extensive coagulation is needed and forceps without any cooling technique are used. This is when the cooling mechanism is mostly desired.

(3) Quantification of the cooling effects of the active heat transfer and SILVERGlide forceps. The model developed in this dissertation can be furthered applied to quantify the cooling effect of the two forceps with cooling techniques.

(4) Expansion of the finite element model to account for the generation of steam and the effect of steam diffusion on tissue temperature and incorporate compression dependent material properties.

(5) Design and manufacturing of a clinical simulator using the tissue-mimicking phantom with embedded thermistors to provide temperature feedback.

(6) Development of the tissue-mimicking phantom material that allows for the control of coagulation temperature and specific heat.